NORTHWESTERN UNIVERSITY

Buried Interfaces in Geological, Biological and Nanoscale Materials

A THESIS

SUBMITTED TO THE GRADUATE SCHOOL
IN PARTIAL FULFILLMENT OF THE REQUIRMENETS

for the degree

MASTER OF SCIENCE

Field of Materials Science and Engineering

By

Michael Jarrett Cohen

EVANSTON, ILLINOIS

August 2014

© Copyright Michael J. Cohen 2014

All Rights Reserved

Dedicated to Ida Saks

TABLE OF CONTENTS

Acknowledgements 7

1 Tomography of Exsolution Processes in Magnetite 12

- **1.1 Introduction 13**
- **1.2 Results 17**
- **1.3 Discussion 31**
- **1.4 Conclusion 37**
- **1.5 Materials and Methods 38**

2 Amorphous Intergranular Phase Controls the Properties of Human Tooth Enamel 46

- **2.1 Introduction 47**
- **2.2 Results and Discussion 50**
- **2.3 Conclusion 63**
- **2.4 Materials and Methods 64**

3 Inorganic-Organic-Inorganic Double-Hybrid Interfaces in Cuprite Nanorod-Gold Nanoparticle Composites 73

- **3.1 Introduction 73**
- **3.2 Results and Discussion 76**
- **3.3 Conclusion 86**
- **3.4 Materials and Methods 86**

4 Characterization of DNA-wrapped CNTs using Atom Probe Tomography 95

- **4.1 Introduction 95**
- **4.2 Results and Discussion 98**
- **4.3 Conclusion 100**
- **4.4 Materials and Methods 101**

References 105

ACKNOWLEDGEMENTS

This work would never have been possible without the support and help of many. First and foremost, I would like to thank my advisor Professor Derk Joester. He first introduced me to the field of dental care, and showed me the potential impact that the application of engineering has in changing oral care. Further, he provided guidance, support and the confidence to take risks, and for that I am forever indebted.

Secondly, I would like to thank my committee members, Professor Lincoln Lauhon and Professor Mark Hersam for their guidance, time, and support through this process.

I thank Dr. Lyle Gordon, for mentoring and guiding me through this process. We had a lot of great success together, and I would never be where I am today without his amazing guidance, persistence and intellect.

I would like to thank the entire Joester group for feedback on presentations, Mathematica code, and posters. I think Michael Whittaker and Emmie Campbell for their feedback on many of my talks and for tolerating my wearing of large headphones to block out disruptions. I would also like to thank Dr. Regina Knapp and Dr. Irene Chang for answering my biology questions. I would like to thank Karen DeRocher for driving me to Argonne to try and grow CNTs and for continuing my work, I look forward to her having great success with all of the projects which are landing in her lap. I would like to thank the Northwestern Materials Science community as a whole. Specifically I thank: Ben Myers for his never ending help with the FIB and SEM; Dieter Isheim for his help

through the years on everything from APT to FIB sample preparation; I would like to thank Carla Shute for assistance with polishing, indentation and more; Jerry Carsello for XRD and XPS assistance; Jinsong Wu and Shuyou Li for TEM help and Eric Wayne Roth for some help with HAADF-STEM.

I also must thank the staff scientists and beamline scientists and the two national labs which helped make this work possible. At Argonne Advanced Photon Source, I'd like to thank Qing Ma, David Vine and David Keaveny for helping with sample preparation, XAS and PEEM respectively. At the Center for Nanoscale Materials, I would like to thank Anirudha Sumant for teaching me how to CVD and putting up with our constant visits; Liliana Stan for help with ALD; and Dan Rosenmann for performing e-beam evaporation deposition on some of my samples. At the Canadian Light Source, I'd like to thank Tom Reiger for helping set up our XAS experiment and coming in to help us at 8am on a Sunday.

I would like to thank my family for their support and encouragement through this process. I especially thank Lindsey, for her love, support, and answering my calls, grumbling that this experiment didn't work or that machine was broken. I thank her for always encouraging me to do my best and for waiting for me to finish my thesis.

Finally, I dedicate this work to Ida Saks, my grandmother who passed away on July 2, 2014. She will always be remembered, and her support of my life, career, and success through her final days will never be forgotten.

Funding for this project was provided by the National Science Foundation (NSF DMR-0805313 and DMR-1106208), the Northwestern University Materials Research Center (NSF-MRSEC DMR-1121262), the International Institute for Nanotechnology, and the National Institute of Health, through a graduate fellowship.

Portions of this work were performed at the DuPont-Northwestern-Dow Collaborative Access Team (DND-CAT) located at Sector 5 of the Advanced Photon Source (APS). DND-CAT is supported by E.I. DuPont de Nemours & Co., The Dow Chemical Company and Northwestern University. Use of the APS, an Office of Science User Facility operated for the U.S. Department of Energy (DOE) Office of Science by Argonne National Laboratory, was supported by the U.S. DOE under Contract No. DE-AC02- 06CH11357, the use of the Center for Nanoscale Materials (CNM), is also an Office of Science User Facility operated for the U.S. Department of Energy (DOE) Office of Science by Argonne National Laboratory, the Canadian Light Source, which is supported by the Natural Sciences and Engineering Research Council of Canada, the National Research Council of Canada, the Canadian Institutes of Health Research, the Province of Saskatchewan, Western Economic Diversification Canada, and the University of Saskatchewan, the Northwestern University Center for Atom Probe Tomography (NUCAPT) supported by NSF-MRI (DMR-0420532) and ONR-DURIP (N00014-0400798, N00014-0610539, N00014-0910781), the Optical Microscopy and Metallography Facility, the Biological Imaging Facility, the Integrated Molecular Structure Education and Research Center, the J. B. Cohen X-Ray Diffraction Facility supported by the NSF- MRSEC (DMR-1121262), the Northwestern University Atomic

and Nanoscale Characterization and Experimental Center (NUANCE) and the Nanoscale Integrated Fabrication, Testing, and Instrumentation Facility (NIFTI) supported by NSF-NSEC, NSF-MRSEC, the Keck Foundation, the State of Illinois, and Northwestern University.

1 TOMOGRAPHY OF EXSOLUTION PROCESSES IN MAGNETITE

This section discusses the use of atom probe tomography to characterize nanoscale exsolution features in spinel-structured oxides, namely magnetite [Fe_3O_4]. Lyle Gordon, Pacific Northwest National Laboratory, whose expertise in choosing samples for experimentation as well as guiding analysis, is recognized. His efforts that instigated this work are noted. Portions of this chapter is in preparation in the form:

> Cohen, M.J., Gordon, L.M., Joester, D. “Tomography of Exsolution Processes in Magnetite”. *in preparation.*

> Godron, L.M., Suram, S.K., Cohen, M.J., Kaluskar K., Rajan, K., Joester, D. “Extracting Crystallographic Information of a Biomineral.” *in preparation*

John Valley, University of Wisconsin: Madison, contributed samples as well as provided geological expertise. Ben Myers, Northwestern University, provided assistance with TEM sample preparation and Nelson Eby, University of Massachusetts: Lowell, contributed the yamaskite samples from which the titanomagnetite was analyzed. Portions of this chapter are also featured in the following:

> Cohen, M.J., Gordon L.M., Suram, S., Kaluslkar, K., Rajan, K., Valley, J.W., Joester, D. Constraining Atom Prove Tomography Reconstructions of Crystalline Oxides. *Microscopy and Microanalysis*. 19 (S2), 1010-1011.

1.1 Introduction

Exsolution of secondary phases from slowly cooled geological formations have found a position of wide spread importance, spanning geothermometry, oxygen geobarometry and geomagnetisim.[4-7] These techniques facilitate the understanding of thermal and environmental changes dating back to planetary nascency. However, conventional attempts to understand critical exsolution processes and their effects on the geological metrology of import are limited in their chemical sensitivity and spatial resolution.

In aluminous magnetites, geothermometry has been previously conducted,[4,6] revealing how exsolution processes and the resulting nanostructured material influences the distribution of $^{18}O/^{16}O$ ratios for use in geothermometric analysis. The genesis of exsolution features is dictated by thermal histories, thus understanding the interplay between isotopic, chemical and microstructural gradients is critical to accurately measure and interpret these records. Nanostructural features alter diffusional pathways, potentially altering oxygen isotopic distributions.[2] These formations have been studied with conventional bright field transmission electron microscopy (BF-TEM) and energy dispersive X-ray spectroscopy (EDS),[2] yet these techniques struggle to provide structural or compositional information in three-dimensions at the nanometer length-scales at which these exsolution features form. Both metrics are critical to fully understand the complex retrograde metamorphism of these types of samples.

Representative of this class of exsolved, aluminous magnetite sample, LP204-1, a magnetite sample hailing from the Adirondack Mountains in New York is characterized.

This polymetamorphic sample has been extensively studied[2,6,8-11] due to its unique, crystallographically oriented, platelet-shaped precipitates. Enriched in Mn, Mg and Al, these platelets formed during a complex retrograde metamorphism and gradual cooling at a rate of 1-3 °C/Ma.[10] Previous experiments by Sitzman *et al.* using BF-TEM[2] reveal that the platelets are oriented along the {100} with coherent interfaces along the length and an incoherent rim at the high curvature edges.

In addition to LP204-1, an exsolved titanomagnetite is characterized. Titanomagnetites possess a wealth of paleomagnetic information, making them one of the most important and widely studied classes of geological formations.[12] In the exsolved form, it is proposed that spinodal decomposition forms a pseudo-lattice of nanoscale, single/pseudo-single domain magnetic, magnetite blocks; engulfed in an ulvöspinel [$TiFe_2O_4$], lamellae-like grid.[5,7,13,14] The magnetic orientation of these single-domain blocks of magnetite hold evidence of the environmental conditions during their formation, providing insight into the paleomagnetic history of earth at the time of exsolution.[14] However, the spinodal decomposition responsible for formation of this nanostructure may alter the magnetic properties as individual domains interact.[5] These exsolution processes have been analyzed via magnetic measurements and electron microscopy, but compositional blind spots remains. Physical separation of magnetite and ulvöspinel in this type of finely structured systems remains nearly impossible due to the size and chemical homologies of the two spinels.[15] While valiant attempts to separate the magnetite blocks from the ulvöspinel using magnetic properties and filtration have been attempted,[15] this nor EPMA[5] are accurate nor provide adequate spatial precision to resolve compositional fluctuations across these precipitated interfaces. To attempt to resolve the compositional character of the spinodal decomposition, a representative, finely exsolved titanomagnetite from Mt. Yamaska in Quebec, Canada is analyzed. The grain's "cloth-like texture"[16] was created by an intrusion described by Nickel[15] which cooled at a calculated rate of 6°C/Ma.[17] TEM conducted by Price[14] suggests that the magnetite blocks bridge to the ulvöspinel matrix with a semi-coherent or coherent interfaces, given by the absence of dislocations.

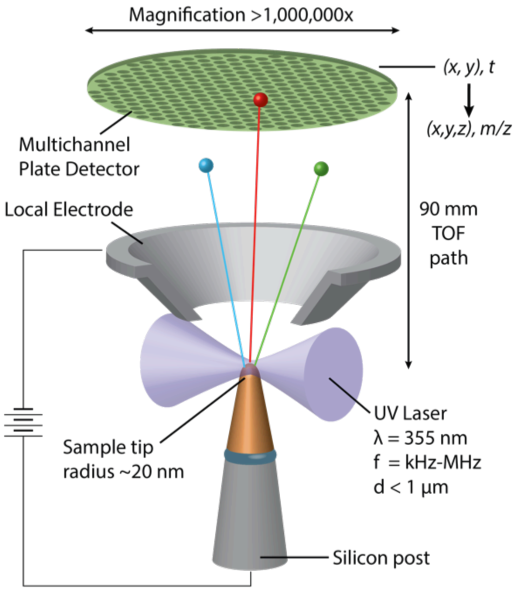
Magnification >1,000,000x
(x, y), t
(x,y,z), m/z
Multichannel Plate Detector
Local Electrode
90 mm TOF path
UV Laser
λ = 355 nm
f = kHz-MHz
d < 1 μm
Sample tip radius ~20 nm
Silicon post

Figure 1.1| Schematic of 3D laser-pulsed atom probe tomography. Sample tip is affixed to a Silicon post with FIB-Pt. Focused UV Laser pulses trigger field emission in the presence of a high electric field. A multichannel plate detector provides (x,y) coordinates, along with time from the laser pulse for time-of-flight (TOF) analysis. Reconstruction parameters allow back-calculation of flight trajectories to reconstruct original sample geometry, atom-by-atom with elemental identification.

In order to advance our understanding of these critical exsolution processes and the potential effect on geological studies, it is pertinent to characterize dimensions and compositional gradients at the nanoscale. Here, the aluminous magnetite and titanomagnetite exsolutions are studied using high angle annular dark field scanning-

TEM (HAADF-STEM), and atom probe tomography (APT). These techniques reveal spatial and compositional information not previously shown by bright field TEM, EDS or EPMA. Atom-probe tomography [Fig 1.1] (APT) has long been used to characterize precipitates and exsolution features at the length scale of 10s of nanometers in metals,[18] but with the advent of ultraviolet laser pulsing,[19] APT analysis of a wide range of dielectric materials is now possible. Briefly, an atom probe is a lensless point projection microscope with magnification better than 10^6.[20] Successive evaporation of ions from a tip—held under a high electric field—are triggered by picosecond UV laser pulses. The evaporated ions are detected by micro-channel plate detector, registering time-of-flight (TOF) and position (x,y). The mass-to-charge ratio and thus chemical identity of each detected ion is determined by TOF. Due to the high ionization potential of this process, numerous molecular fragments and charge states are observed, yet these do not necessarily have a bearing on the native coordination of the cation or anion within the sample. As this is a TOF technique, compositional and isotopic information is recorded.[21] The multi-channel position sensitive detector provides imaging of the sample via reconstruction algorithms. Generally, atom probe tomography allows for reconstructions of three-dimensional volumes of sample atoms with a positional accuracy of roughly 0.3-0.5 nm[20] with parts-per-million chemical sensitivity across the periodic table. Atom probe has a history of analyzing both geological[8] and biological[22] magnetite and has shown both chemical and tomographical precision in this material system.

Here, two exsolved magnetite specimens are characterized with atom probe tomography and HAADF-STEM. First, a magnetite crystal, which has undergone polymetamorphism—designated LP204-1—with Al, Mg and Mn enriched platelets. This specimen and locality have been studied with TEM and EDS,[2] micro-indentation,[23] SIMS,[6] field ion microscopy and even atom probe tomography.[8] While previous studies with atom-probe tomography have been undertaken, the lack of a pulsed-laser gave limited results and no tomographical information.

The second specimen is an exsolved, ulvöspinel-magnetite, spinodal decomposition with a matrix of ulvöspinel surrounding a pseudo-lattice of magnetite cuboidal blocks from Mt. Yamaska, Quebec. This class of titanomagnetite sample has also been studied using TEM, EPMA,[14] magnetic force microscopy, electron holography[7] and variable field translation balance.[13] While all of these techniques have provided major scientific advances, none has provided the compositional and tomographical description which atom probe tomography is capable.

1.2 Results

Conventional bright field transmission electron microscopy (BF-TEM) and high angular annular dark field scanning-TEM (HAADF -STEM) was conducted on thin sections of LP204-1 prepared with focused ion beam lithography. Samples were tilted to the [100] zone axis [Fig 1.2, inserts]. BF-TEM [Fig 1.2a] image contrast is dominated by contributions from lattice strain (Ashby-Brown or “coffee-bean” contrast) associated with the platelets. HAADF-STEM image contrast, on the other hand, is largely from atomic-number (Z-contrast).[24] This image shows dark, thin platelets aligned orthogonally to each other and aligned along the {100} direction.

Dimensions and area fraction of platelets were determined from the HAADF-STEM images. The average width of the precipitates is 11.3±2.0 nm at full-width half maximum along background-corrected image contrast line scans ($N_{\text{platelets}}$ =12). The length of long-axis ranges from 22 nm to 141 nm. Little to no correlation is found between observed axis and width for precipitates in HAADF imaging. The precipitate area fraction 8.34±0.79% was determined using contrast-based thresholds.

BF-TEM of titanomagnetite thin sections tilted to the [100] zone axis shows cube-shaped high-contrast features separated by thin lamellae. This image is similar to those found in the literature, which describes exsolved Mt. Yamaska titanomagnetite samples.[14] This image is characteristic of magnetite cuboids and thin lamellae of ulvöspinel [Fig 1.2c]. Typical of micrographs of this sample found in the literature, contrast varies throughout the sample, suggesting compositional or thickness variations.

Dimensions and area fraction of magnetite blocks were determined from the HAADF-STEM images. The length of the cuboids ranges from 17 nm to 48 nm. Little to no correlation is found between observed axis and width for precipitates in HAADF imaging. The precipitate area fraction 47.84±1.37%, was determined using ImageJ contrast-based threshold.

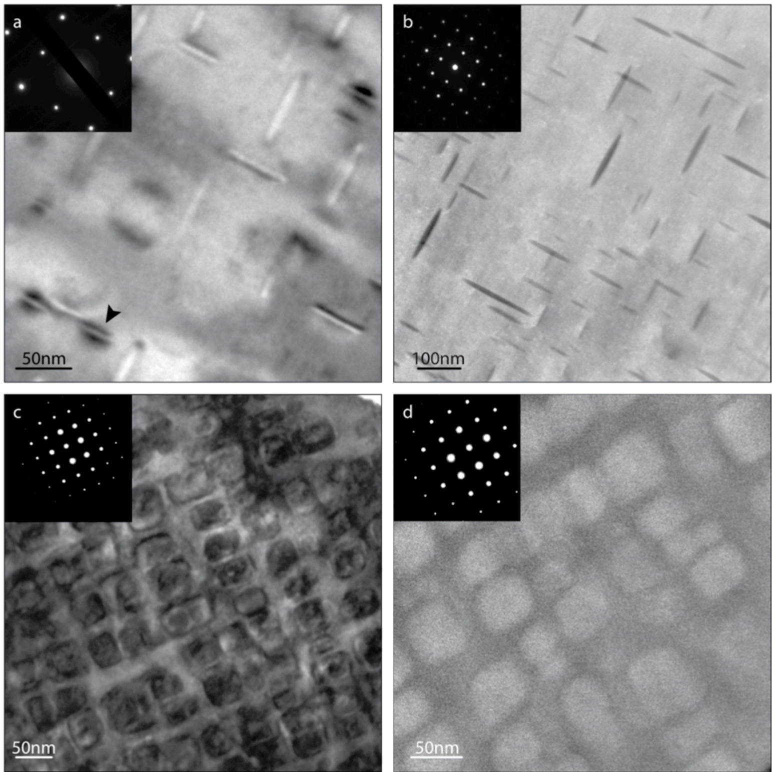

Figure 1.2|(inset shows corresponding diffraction pattern, all images taken at the [100] zone) a| Conventional BF-TEM of LP204-1, arrow designates Ashby-Brown strain contrast; b| HAADF-STEM of LP204-1 showing predominately Z-contrast and low-Z platelets; c| Conventional BF-TEM of titanomagnetite, showing a mixture of concentration and strain contrast; d| HAADF-STEM of titanomagnetite, showing predominately Z contrast, outlining the magnetite blocks.

Atom probe runtime parameters (laser power, 0.5 pJ; detection rate, 0.005 ions per pulse; pulse repetition rate, 500 kHz; and a base temperature, 35 K) were optimized specifically for magnetite samples. Briefly, laser power settings were chosen to maximize stoichiometric accuracy and decrease background. We find that at lower laser powers (.1-2 pJ) more oxygen is detected [Fig 1.3d], improving the relative atomic percentage of Mn, Mg, Al in LP204-1 as compared with EPMA [Fig 1.3a].[2] However, extremely low laser powers (~0.1 pJ) are associated much higher background levels [Fig 1.3b]. The laser power of 0.5 pJ was chosen as it provides reasonably accurate stoichiometric information, while balancing spectrum background noise levels.

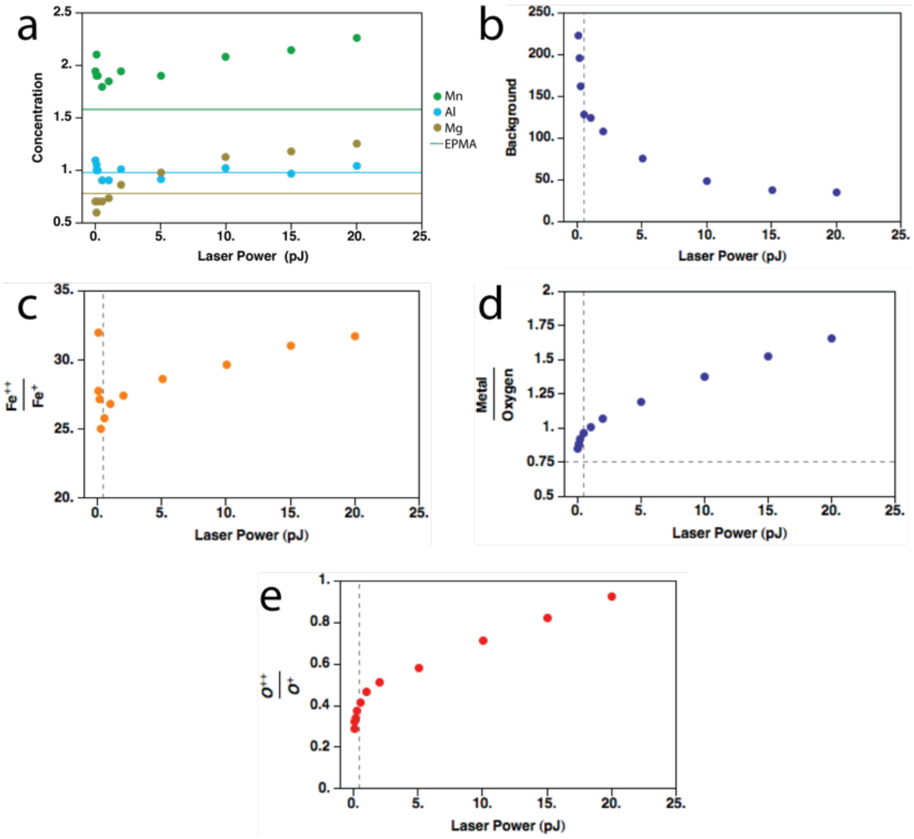

Figure 1.3| (in all plots, vertical dashed line is located at selected 0.5 pJ laser power) a| Concentration (at%) of three appreciable minority constituents in LP204-1 as measured by APT compared to EPMA data[2]; b| Background (ppm/nsec) measured for LP204-1 against laser power; c| Charge State Ratio (CSR) for iron compared to laser power for LP204-1; d| Metal to Oxygen ratio for LP204-1 against laser power, horizontal line placed at M:O of 0.75, assumed for spinel structure of magnetite; e| CSR for Oxygen for LP204-1 as measured against laser power.

Atom probe mass spectra of LP204-1 and titanomagnetite samples share a number of features [Fig 1.4]. For both samples the doubly charged monatomic ions [Table 1.1] dominate; except in the case of Ti in the titanomagnetite where Ti is spread across Ti^+ and $TiO_yH_x^{z+}$; where $x = 0\text{-}1$, $y = 0\text{-}3$, and $z=1\text{-}2$. Note that $TiO_3H_0^{2+}$ is not considered as it overlaps with Ti^+. A considerable number of metal oxide molecular ions were detected, especially for Fe, Mn, Ti and Al. For a comparison, see Table 1.1 for relative abundances.

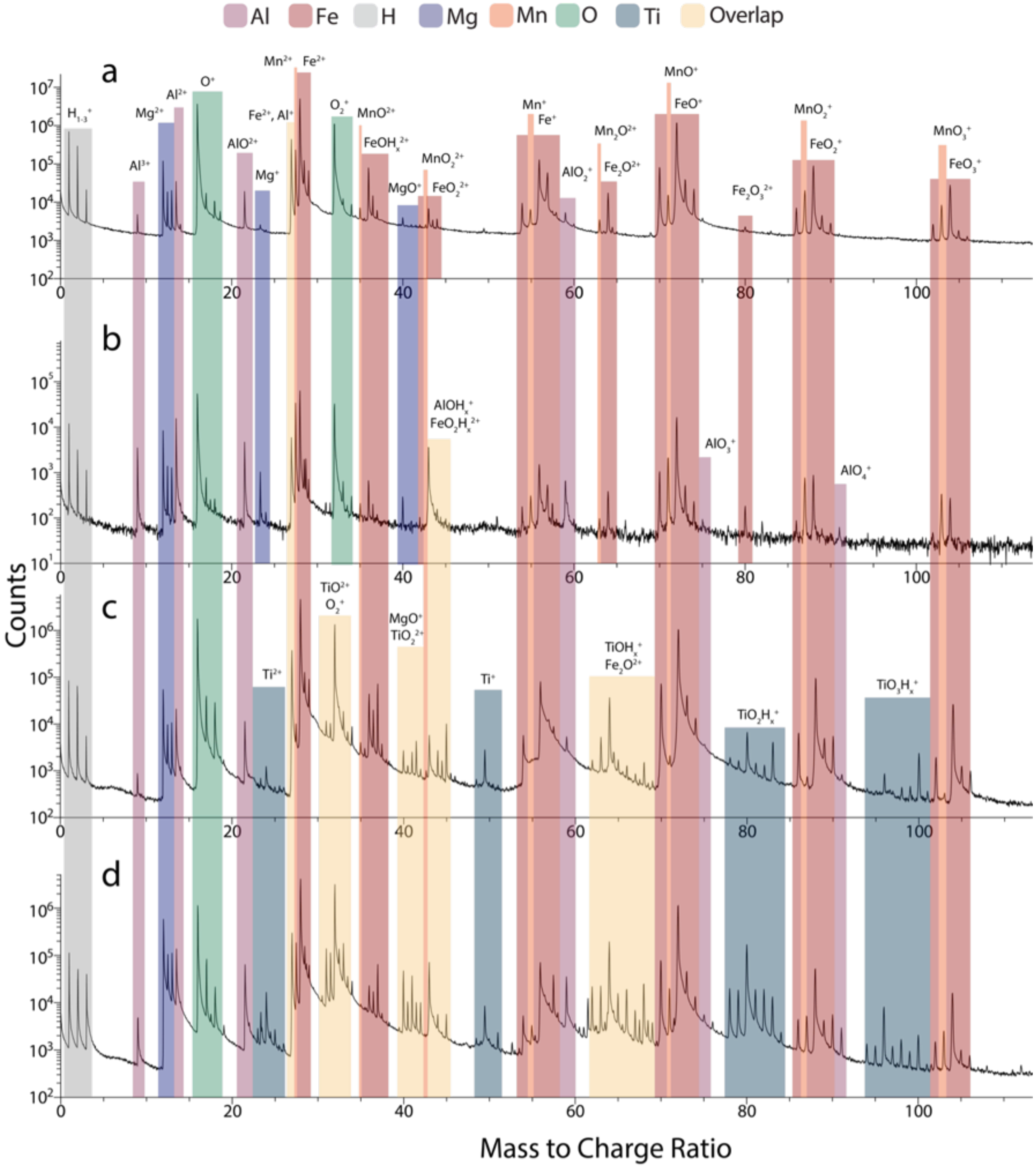

Figure 1.4| Atom probe spectra color coded for metal, oxygen or hydrogen with overlaps designated: a| LP204-1 matrix (χ Al ≤ 1.2 at%); b| LP204-1 platelets (χ Al ≥ 1.5 at%); c| Magnetite blocks (χ Ti ≤ 4.2 at%); d| Ulvöspinel matrix (χ Ti ≥ 4.5 at%)

Qualitative inspection of 3D reconstructions of atom probe data sets indicates that precipitates in LP204-1 are enriched in Al, Mg and Mn compared to the surrounding magnetite matrix [Fig 1.5a]. In the Mt. Yamaska titanomagnetite, magnetite precipitates are depleted in and the surrounding ulvöspinel is enriched in Al, Mg, Mn and Ti [Fig 1.5b]. For compositional analysis, precipitates in LP204-1 are defined as any volume where the aluminum mole fraction $\chi_{\mathrm{Al}} \geq 1.5$ at% and the magnetite matrix as any volume with $\chi_{\mathrm{Al}} \leq 1.2$ at%. In the titanomagnetite, the Ti-rich ulvöspinel matrix is defined as any volume with $\chi_{\mathrm{Ti}} \geq 4.5$ at% and the magnetite nanoparticles are identified by $\chi_{\mathrm{Ti}} \leq 4.2$ at%. The composition of matrix and precipitate was then determined by integrating mass spectra for the matrix and precipitate [Table 1.2]. In LP204-1, the partition coefficients, defined as the difference between the log of platelet atomic percent and the log of matrix atomic percent, log $P_{\mathrm{platelet/matrix}}$ are 0.71 for Al, 0.39 for Mg and 0.67 for Mn. In titanomagnetite, the partition coefficients log $P_{\mathrm{ulvöspinel/magnetite}}$ are 0.36 for Al, 0.72 for Mg, 0.55 for Mn and 0.41 for Ti.

	Element	Order Relative Abundance (top 5)				
LP204-1	Fe	Fe^{2+}	FeO^{+}	Fe^{+}	FeO_2^{+}	FeO^{2+}
	Al	Al^{2+}	Al^{+}	AlO^{2+}	Al^{3+}	AlO_2^{+}
	Mg	Mg^{2+}	Mg^{+}	MgO^{+}		
	Mn	Mn^{2+}	MnO_2^{+}	MnO^{+}	Mn^{+}	MnO_2^{2+}
	O	O^{+}	O^{2+}			
Yamaskite	Fe	Fe^{2+}	FeO^{+}	FeO_2^{+}	Fe^{+}	FeO^{+}
	Al	Al^{2+}	Al^{+}	AlO_2^{+}	Al^{3+}	AlO_2^{+}
	Mg	Mg^{2+}	MgO^{+}			
	Mn	Mn^{2+}	MnO_2^{+}	MnO^{2+}	MnO_2^{+}	MnO^{+}
	O	O^{+}	O^{2+}			
	Ti	TiO^{+2}	TiO^{+}	TiO_2^{+}	Ti^{2+}	Ti^{+}

Table 1.1 Relative peak counts for the various ionic and molecular fragment contributions for each element found in both the LP204-1 sample as well as the Yamaskite sample.

Element	Atomic %	Cation fraction
LP204-1	Matrix	<1.2 at% Al
Al	0.29	0.02
Fe^{2+}	44.42†	0.86
Fe^{3+}		1.98
Mg	0.65	0.04
Mn‡	1.58	0.10
LP204-1	Platelets	>1.5 at% Al
Al	4.32	0.30
Fe^{2+}	29.74†	0.37
Fe^{3+}		1.70
Mg	2.01	0.14
Mn‡	7.08	0.49
Yamaskite	Ulvöspinel Matrix	>4.5 at% Ti
Al	2.54	0.15
Fe^{2+}	36.45†	1.20
Fe^{3+}		0.94
Mg	2.89	0.17
Mn‡	1.46	0.09
Ti	7.80	0.46
Yamaskite	Magnetite Blocks	<4.2 at% Ti
Al	1.10	0.06
Fe^{2+}	48.62†	1.12
Fe^{3+}		1.60
Mg	0.53	0.03
Mn‡	0.40	0.02
Ti	3.02	0.17

Table 1.2| Atomic percentage and cation fraction for matrix and Exsolution features for both LP204-1 and yamaskite †atomic percentage of iron reported together for both charge states; ‡Mn is assumed to be divalent

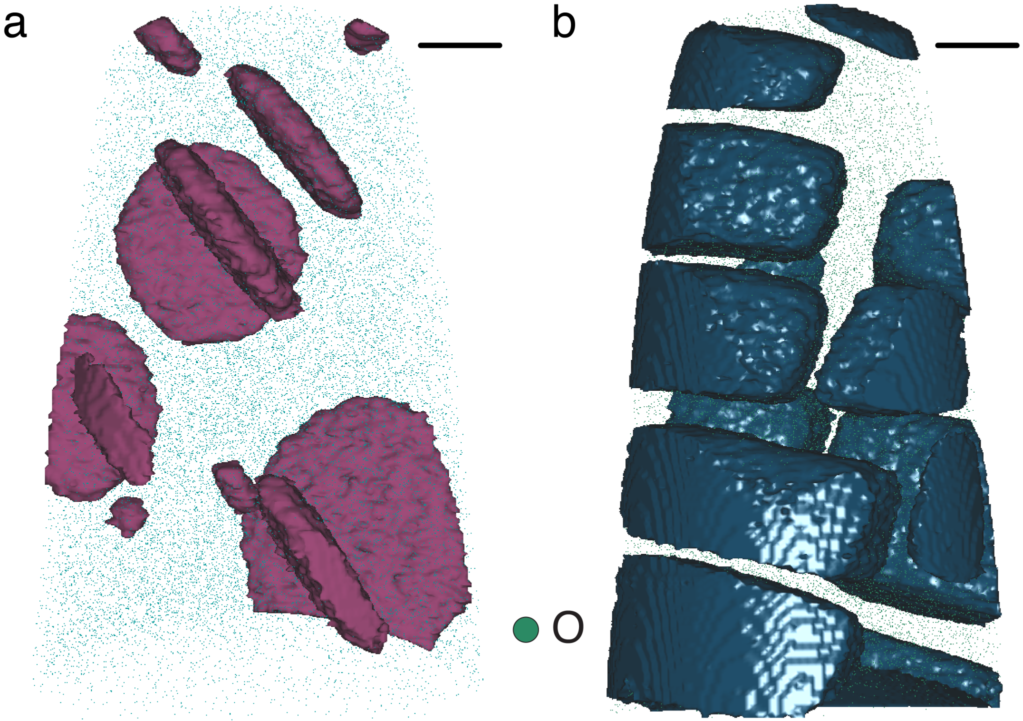

Figure 1.5| APT reconstruction visualizations of (a) LP204-1 with platelets highlighted by Al isoconcentration surfaces (χAl = 2.5at%); (b) Magnetite blocks in titanomagnetite by Ti iso-surfaces (χTi = 2.8at%). In both reconstructions, 0.5% O (16 Da peak) is visualized to demonstrate overall sample shape. (scale bar is 20 nm)

Precipitates in LP204-1 have a slightly oblong disk shape [Fig 1.5a], oriented along the {100}. Spatial analysis of Al-rich platelets in LP204-1 reconstructions reveals an average thickness of 9.05±1.48 nm (N=10), an average aspect ratio of 1.23±0.05, with the longest axis ranging from 12-55 nm (N≈8, including platelets extending outside the volume analyzed by APT). Platelets account for a volume fraction of 6.7% (v/v) across all samples ($V_{\mathrm{platelets}}$= 4.10×10^4 nm^3) with a number density of ~9500 platelets/μm^3.

Magnetite block-shaped precipitates in titanomagnetite are block-shaped with rounded corners [Fig 1.5b]. The blocks account for a volume fraction of 43.7% (v/v). The longest dimension of blocks inside the analytical volume ranges from d = 31-74 nm (N=15).

Compositional profiles of platelets in LP204-1 [Fig 1.6a] exhibit a Gaussian-like shape, spreading through the interface to the matrix. Profiles across individual platelets in LP204-1 reveal that Mg, Mn and Al are graded over 3.5 nm [Fig 1.6a]. These minorities climb within the platelet with a global average of 7.08±0.71 at% Mn; 4.32±0.49 at% Al, 2.01±0.39 at% Mg [Fig 1.5b] (*N*=10). Within the platelet, the iron composition drops to a global average of 29.74±1.22 at% [Fig 1.7a] (*N*=10).

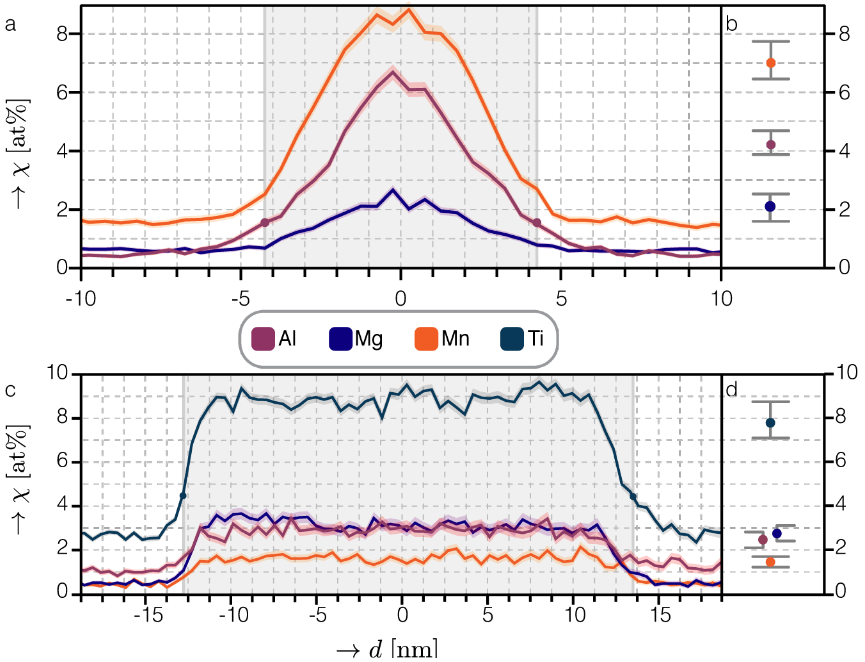

Figure 1.6| Platelet Concentration Profiles shown for representative exsolution features with error bars shown by opaque widths on either side of the solid atomic percentages, feature widths are defined by grey boxes where Al or Ti dot represents atomic percent cutoff for LP204-1 and Titanomagnetite exsolution features, respectively; a| Representative LP204-1 Platelet with concentration profile shown for Al, Mg and Mn; b| Boxplot for global platelets with average mean and extreme concentration values shown; c| Representative Ulvöspinel exsolution concentration profile shown for Ti, Al, Mg and Mn; d| Boxplot for global ulvöspinel concentration profiles averages with mean and extreme values shown for each element.

Similarly, concentration profiles across the ulvöspinel matrix between magnetite blocks in titanomagnetite samples show a graded interface where Ti, Mn, Mg and Al increase to global averages within the ulvöspinel to 7.80±0.73, 1.46±0.16, 2.89±0.34, and 2.54±0.22

at% respectively. As in the case of the LP204-1 platelets, the iron concentration necessarily decreases [Fig 1.7b] within the exsolved feature to a global average of 36.45±1.96 at% from measured magnetite atomic percent of iron at 48.55±0.78 at%. The minority constituents increase from the magnetite block where the average composition for Ti, Mn, Mg and Al are 3.05±0.14, 0.41±0.03, 0.55±0.06, and 1.11±0.07 at% respectively (*N*=7).

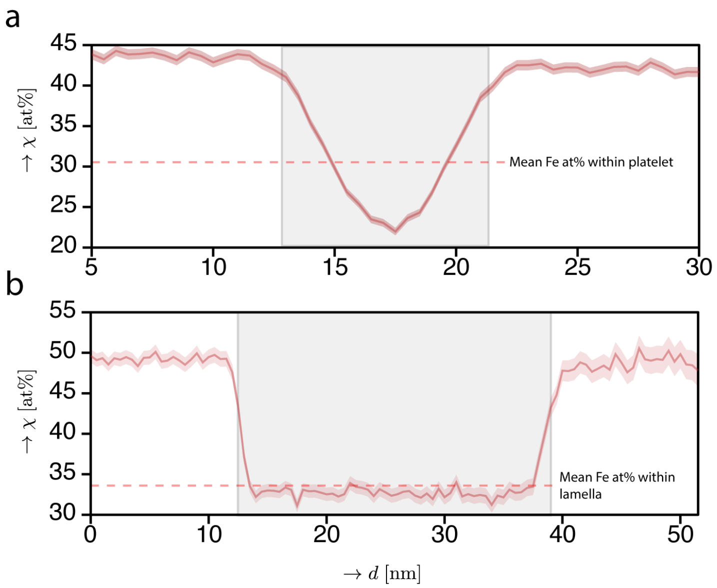

Figure 1.7| a| Platelet Concentration Profile for LP04-1 for Fe (as in Fig 1.6a) with mean platelet iron composition shown; b| For Yamaska (as in Fig 1.6c) with mean lamella Fe composition shown.

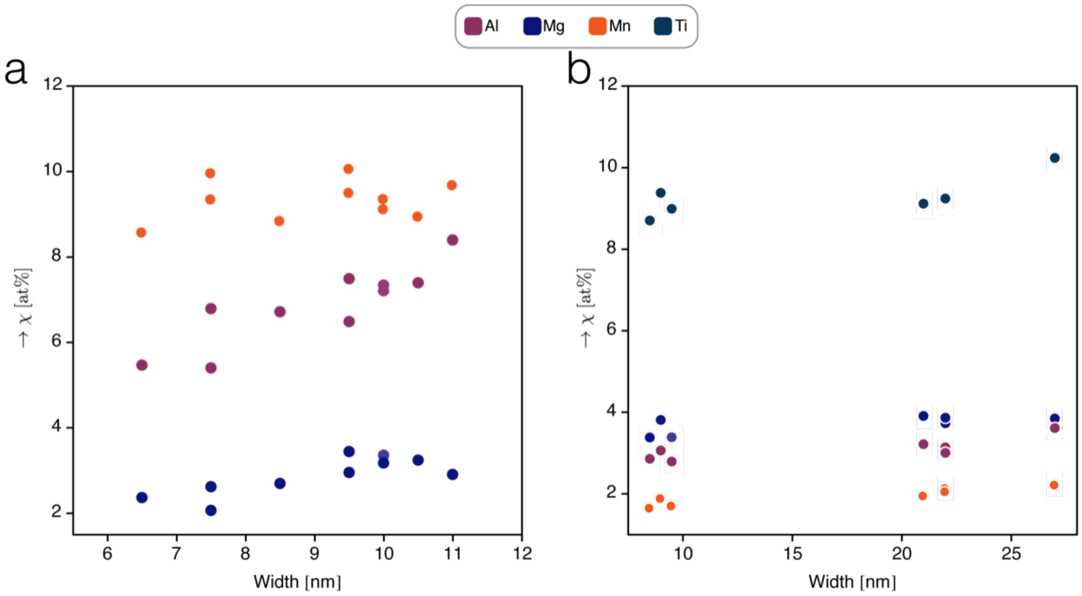

Figure 1.8| Platelets and lamellae [a and b; respectively] maximum atomic composition compared with the measured width of the exsolved feature.

There is a general increase in maximum atomic percentage of minority elements as compared to width of exsolved feature. In the case of LP204-1 [Fig 1.8a], a loose, but general trend of increase in Al, Mg, and Mn is found. By considering the composition vs. width plot and the platelet profiles, we can hypothesize that the maximum observed platelet compositions for Mg, Al, Mn (3.41, 8.37, 10.04 at%, respectively) are suggestive of the solubility limit of these minority elements in this system. In the titanomagnetite system many, thick, lamellae exist with widths greater than 20nm display apparent solubility limits [Fig 1.6c, 1.7b]. These maximum concentration values are 10.21, 2.19, 3.88 and 3.58 at% for Ti, Mn, Mg and Al respectively.

A non-negative least squares fitting approach[25] was used to express the composition of the bulk samples and exsolved phases in terms of spinel-type endmembers. For LP204-1, the optimal fit to the following endmembers was utilized: magnetite [Mag, Fe_3O_4], spinel

[Sp, $MgAl_2O_4$,, jacobsite [Jac, $MnFe_2O_4$], and galaxite [Glx, $MnAl_2O_4$] [Fig 1.9a,b]. The endmembers selected for the titanomagnetite samples were magnetite, magnesioferrite [Mgf, $MgFe_2O_4$], ulvöspinel [Ulv, $TiFe_2O_4$], and galaxite [Fig 1.9c,d]. The mean platelet composition in LP204-1 is $Mag_{19}Sp_{18}Jac_{60}Glx_3$. The mean matrix composition, $Mag_{87}Sp_2Jac_{12}Glx_0$ is very similar to the overall composition of the sample, $Mag_{84}Sp_4Jac_{12}Glx_0$. The titanomagnetite sample had an overall composition equivalent to $Mag_{47}Ulvö_{34}Mgf_{14}Glx_5$ Magnetite blocks were predominantly magnetite, $Mag_{97}Ulvö_5Mgf_4Glx_3$, the Ti-rich lamella however were closer still in composition to magnetite than to ulvöspinel, $Mag_{29}Ulvö_{46}Mgf_{17}Glx_8$.

In both magnetite-containing specimens examined; the matrix, exsolved feature and geological specimen are all found to lie generally on a tie line. In the case of LP204-1 [Fig 1.9b], there is a clear congregation of larger (10-11 nm) platelets around an average value. While outliers exist, three platelets of smaller widths (6.5 to 9.5 nm) can be seen to lie clearly along the tie line between the matrix and the exsolved phase. This is suggestive that these platelets have not fully coarsened to maximum solubility concentration and dimensions.

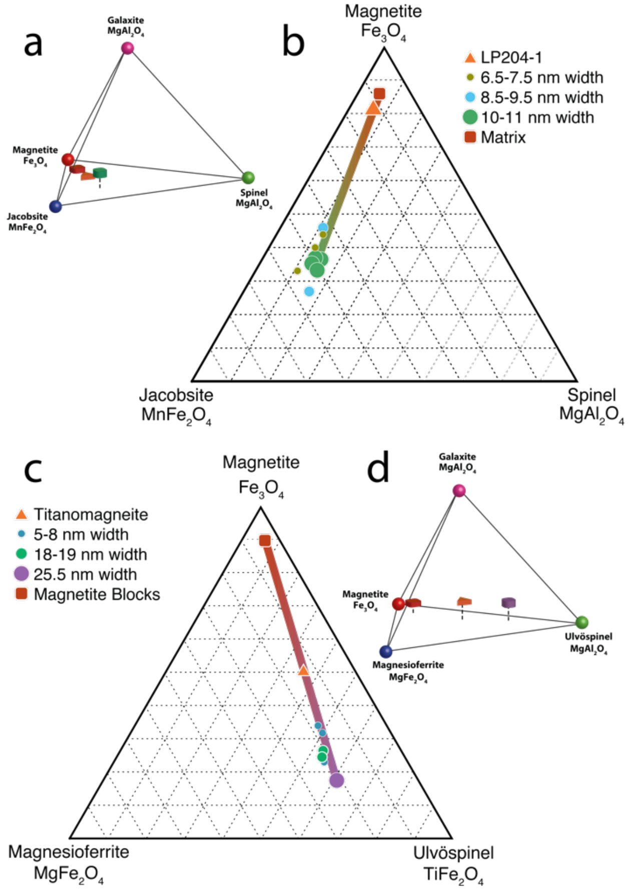

Figure 1.9| Exsolution features and matrices plotted on appropriate Ternary diagrams, a| Shows the 3-D tetrahedron diagram with 4 endmembers, this is projected down onto the Magnetite-Jacobsite-Spinel plane as shown in b| where all analyzed platelets are displayed, size and color of circle corresponds to the platelets width, LP204-1 and the matrix are also rendered, with a tie line connecting to the largest platelet. Similarly, d| shows the 3-D tetrahedron with 4 endmembers and is shown in project in c| in the Ternary diagram form for the titanomagnetite, the width of the ulvöspinel lamellae is rendered relative to the size and color of the appropriate circle. The entire specimen and magnetite blocks are rendered with the appropriate tie line.

In the lamellae of the titanomagnetite specimen [Fig 1.9c.], the largest lamellar of ulvöspinel (25.5 nm in width) demonstrates compositional character most similar to pure ulvöspinel. While thinner lamellae lie along the tie line between nearly pure magnetite blocks and coarsest lamellae.

1.3 Discussion

With the advent of ultraviolet laser atom probe tomography, analysis of a wide range of dielectric materials is now possible.[19,26] The ability to characterize more than just metals and highly doped semiconducting materials gives APT the potential to influence new fields and answer questions that previous techniques are ill equipped to address. Here, we demonstrate the potential of APT in characterizing geological oxide materials. While previously oxides and glasses have been explored,[22,27-31] of interest here is how exsolution features with dimensions on the nanoscale affect geological measurements such as geothermobarometry, oxygen isotope gradients and paleomagnetism.

When first characterizing a new material with APT, it is critical to consider runtime parameters. These may vary with sample preparation, conductivity and composition. Further, these runtime parameters are found to have a direct effect on the following (in order of import): throughput, measured stoichiometry, spectra background and relative charge state peak intensities. When optimizing runtime parameters, the interplay of these experimental results is important to consider while augmenting. Here, we optimized laser power by choosing a value (0.5 pJ) that would maximized sample yield and stoichiometry. Generally oxide samples fail in the atom probe at a rate of 10-40%, depending on material, sample preparation expertise and user experience level. As the background or noise level is found to decay exponentially with laser power, it would be reasonable to increase laser power to decrease the background level. This occurs due to a decrease in operating accelerating voltage which decreases direct current evaporation.[32] However, at higher laser powers, the metal to oxygen ratio is found to increase due to a decrease in detected oxygen. Therefore, in order to minimize background while reaching accurate stoichiometry, a laser power of 0.5 pJ was chosen. While atom probe tomography is considered a quantitative, standard-less technique, the use of standards or correlation with electron microprobe can be very useful in optimizing atom probe runtime parameters, especially when considering complex oxides and silicates.

When characterizing complex oxides with this technique, we expect a number of single ions as well as metallic-oxide fragments.[33] In the case of Fe, Mg, Al and Mn, we observe the dominance in the spectrum of the 2+ peak, which is consistent with previous analyses of similar transition metals, alkaline earth metals, post-transition metals and metalloids in magnetite,[22] hematite,[34] nickel oxide,[26] apatite,[27] silicon in zircons,[30] calcite,[35] silicon dioxide and saphire.[36] There are a number of complex oxygen-containing molecular fragments as well, and while in iron, these follow a logical FeO^+, FeO_2^+, FeO_{3+} sequence as seen previously,[22] the other metallic oxide peaks follow less clear trends [Table 1.2]. Titanium moves away from the trend of the other transition metals. In titanium, it is found that TiO^{2+} makes the strongest contribution. Considerable overlap is found in TiO^{2+} and TiO^+ due to the presence of oxygen and iron. Further work is needed with atom probe tomography to characterize titanium ceramics such as rutile and titanium based silicates.

When analyzing spectrum, a few additional concerns must be noted. Firstly, the appearance of hydrogen-containing ions must be considered. For example, in the titanomagnetite sample, numerous hydrogen-containing ions are uncovered. However, hydrogen contamination in the vacuum system and metal walls is a commonly known[36] and researchers in the field are considering glass linings inside the vacuum chamber to minimize this artifact. Secondly, overlaps between elemental ions and molecular fragments must be considered. For example, Al^+ and $^{54}Fe^{2+}$ overlap at 27 Da, and TiO^{2+} and O_2^+ at 32 Da. Calculating the expected contribution due to natural isotope ratios might assist with decomposing these spectral overlaps. However, if isotope analysis is unknown, complementary experiments must be employed to confirm abundance ratios. Further, if measurements of slight deficiencies in isotopes are of interest, these cannot be used to reconcile spectral overlap. For these reasons, careful attention must be taken to identify and avoid (if possible) peak overlap. Finally, multi-hits should be considered. The occurrence of multiple evaporation events incident on the detector within one detection time window (Δt) can lead to misinterpretation of spectrum.

Proper reconstruction of atom probe tomography data allows for very accurate dimensional analysis. Unobstructed by strain contrast (BF-TEM), imprecise zone alignment (TEM) or thermal drift (TEM), atom probe can generally recreate sample architecture with impressive spatial precision. While atom probe does have slight imprecisions in spatial determination, it is generally quite accurate. In the *z*-direction, the imprecision arises out of the random probabilities of field evaporation for atoms within a given thin shell and is found to be between 0.02 - 0.06 nm.[32] Lateral resolution ($\Delta x, \Delta y$) is less well defined in the literature, is generally related to thermal agitations created by the laser,[37] trajectory aberrations,[38] or atom movement along the tip surface (so-called "roll-up").[32]

This spatial accuracy, combined with elemental sensitivity allows for incredibly precise determination of exsolution features size and dimensions. Previous work with BF-TEM and LP204-1 reported that the width of the platelets is 1-3 nm.[2] Dimensions determined from HAADF-STEM and APT differ greatly from the literature values because these experiments define the dimensions of the platelet by a Z-contrast or chemical gradient, respectively. In BF-TEM, determining size via the complex contrast observed due to the combined influence of mass-thickness and lattice strain can be precarious. However, platelet mean number density can accurately be determined from BF-TEM because each coherent platelet creates a unique strain field, immediately recognizable in BF-TEM. Remarkably, in APT when analyzing an incredibly small volume, we are able to determine a number density of 9500 platelets /μm^3. This density is almost exacting to that determined by BF-TEM previously 10^4 platelets/μm^3.[2] This exemplifies the degree of homogeneity of the exsolved features found in this type of magnetite sample, which makes APT a very promising technique to characterize these types of samples.

Similar area approximations have been made for exsolved titanomagnetites in the literature using conventional TEM. Nickel found that the ulvöspinel occupies 68.4% by area from point counting on TEM images.[15] Similarly, Price concluded a volume ratio of 48:52 between ulvöspinel and magnetite.[5] These inconsistent ratios reveal the local variation in size and shape of the lamellae and blocks. In this study, two nearby grains were studied with HAADF-STEM and APT, which yields ratios of 45:55 by area and 56:44 by volume respectively. To properly correlate these values, it could have been possible to perform TEM on the APT sample prior to APT evaluation. Even though all reasonable attempts were made to characterize nearby grains, it is apparent from the variation in numbers that local variations within and between grains occurs.

From analysis of the compositional profiles [Fig 1.6, 1.7], we observed segregation of trace cations into the LP204-1 precipitates. From comparison of the partition coefficients, it is apparent how much stronger Al and Mn are segregated than Mg. The matrix has exsolved nearly all of the trace elements into the platelets with only 3.13 at% remaining in the matrix. Prior work with TEM-EDS, showed that these platelets were exhibit a galaxite or hercynite-like [$FeAl_2O_4$] compositions[2] because of the inability to detect the Mg present within the platelets. Upon inspection, our data reveals the appreciable amounts of Mg (2.2 at%). This technique featured here show that the platelets exhibit predominately Jacobsite-like compositional character. Electron microprobe analysis (EPMA) gives an overall chemical formula of $Mn_{.113}Mg_{0.056}Fe^{2+}_{0.831}Al_{0.070}Fe^{3+}_{1.930}O_4$,[2] which is nearly exactly concurrent with overall composition found by APT:

$Mn_{.114}Mg_{0.051}Fe^{2+}_{0.833}Al_{0.073}Fe^{3+}_{1.927}O_4$. This exhibits the compositional accuracy, even when sampling a nanoscale sample volume.

Previous work in the titanomagnetite system with BF-TEM suggests that the contrast variation may result from compositional variations.[14] However, the variations probed by BF-TEM would appear to exist on a larger wavelength than those observed in APT. While it has proven to be extremely difficult to physically or chemically separate the ulvöspinel from the magnetite blocks, valiant efforts to do compositional analysis have been done by Nickel. Nickel's first attempts are based on approximating the area percentage (via electron micrograph) and assuming that the block-like precipitates are pure stoichiometric magnetite. This approximation yields a chemical formula of $Ti_{.71}Mg_{.42}Fe^{2+}_{.58}Al_{.26}Fe^{3+}_{1.03}O_4$ for the ulvöspinel matrix. This is similar to the results yielded by APT, which gives a chemical formula of $Ti_{.58}Mg_{.22}Fe^{2+}_{1.36}Al_{.10}Fe^{3+}_{0.73}O_4$. These values are similar to EPMA data from ulvöspinel from the Nass River Valley locality ($Ti_{.73}Mg_{.10}Fe^{2+}_{1.60}Al_{.06}Fe^{3+}_{0.46}O_4$).[39] More recent compositional analysis on the same specimen was carried out with EPMA, determining a chemical formula of $Ti_{.37}Mg_{..07}Fe^{2+}_{1.39}Al_{.10}Fe^{3+}_{1.06}O_4$. However this technique is unable to resolve variation between lamellae and precipitate. Previous efforts have attempted to isolate the ulvöspinel mechanically, yet this has proven to be essentially impossible due to size and the coherent nature of the interfaces.[15] Similarly, acid separation has shown to be equally as futile due to the chemical similarities of the spinels.[15] Magnetic separation has showed some promise, but can't fully isolate the mixtures and the chemical analysis techniques of the time can't isolate Fe from Mn completely.[15] The similarity of the ulvöspinel lamellae to the Nass River Valley ulvöspinel would suggest that this exsolved feature is approaching solubility limits for this spinel, further suggested by the plateau observed in the compositional profiles [Fig 1.6c].

Isotope gradients through grains of materials are commonly probed using secondary ion mass spectrometry (SIMS) to detect local changes of isotope ratios for oxygen geothermometry. No segregation of gradients of oxygen or other isotopes was found in this sample. As described elsewhere, oxygen can be very difficult to accurately resolve in atom probe oxide samples, resulting in a myriad of deleterious results that would make $\delta^{18}O$ gradient resolution difficult: oxygen deficiency,[26,34] $^{18}O^{+}/H_2{}^{16}O^{+}$ overlap and $^{16}O_2{}^{2+}/^{16}O^{+}$ overlap. While atom probe tomographic measurement of isotope ratios has been used to confirm ages of zircons,[21] we are simply able to confirm the terrestrial origins of the grains studied. However, future correlative efforts with oxides to examine oxygen isotope ratios over larger length scales may be useful to compare with traditional techniques for geothermobarometry.

1.4 Conclusion

No technique rivals atom probe tomography's combination of spatial resolution and chemical sensitivity. So-called "nanogeology"[40] caries promise to unravel terrestrial and extraterrestrial[41] mysteries. Further, atom probe possesses the capacity to further our understanding of geobarometry, geothermometry and geomagnetism at the nano-scale. While traditional techniques such as SIMS operate at a much larger length scales, information at smaller length scales become relevant with the presence of nanoscale compositional heterogeneity.

We must however recognize the limitations of the technique. Firstly, careful consideration of reconstruction parameters must be undertaken in order to draw any reasonable conclusions regarding dimensionality. Secondly, like any technique, systemic errors potentially exist. Here we observe gross inaccuracies in isotopic measurements, begging for further, standardized study in order to enable further use of atom probe tomography in the field of isotopic and trace element geochemistry.

Magnetite is one of the most common materials on earth giving it a special stance in the study of biology,[42,43] geology, astrogeology,[44] and even astrobiology,[45] We have now successfully shown the ability of atom probe to gain useful insight at the nanoscale in biological[22] and geological magnetites. With this successful intrusion into geological oxides, this work and others[21] sets the stage for continued application of atom probe tomography in the analysis of silicates and other interesting geological formations.

1.5 Materials and Methods

1.5.1 Materials

LP204-1 is a geological magnetite crystal from a polymetamorphised, granulite-facies marble[11]. This samples originates from the Weston Mines Skarn in N.E. Mt. Marcy Quadrangle of the Adirondack Mountains, New York, USA.

Titanomagnetite is from a yamaskite rock, which originates from Mt. Yamaska in the Monteregian Hills in Quebec, Canada.

Two homogenous mineral standards were also analyzed: galaxite from Bald Knob (North Carolina, USA) and octahedral magnetite single crystals from an unknown locality.

1.5.2 Sample Orientation

LP204-1 crystals were mounted to glass cover slips using wax mounting adhesive (Crystalbond 509). Samples were irradiated with an Mo X-ray source in a custom Laue backscatter diffraction set-up, operated at 25 kV and 11 mA. Diffraction patterns were recorded on photostimulable phosphor image plates and scanned with a Molecular Dynamics Storm 860 phosphoimager (GE Healthcare). Diffraction patterns were compared to simulated patterns (CrystalDiffract 6, CrystalMaker Software Limited) to identify samples aligned within ~10˚ of the desired crystallographic zone axis ([111] and [100]).

1.5.3 Mounting, grinding and polishing

Appropriately oriented crystals were then embedded in epoxy resin (Epo-Tek 301) and cured overnight at 25°C. Embedded samples were ground using progressively finer grits of Buehler SiC grinding paper (400, 600, 800 & 1200 grit) and polished using 3 and 1 μm polycrystalline aqueous diamond polishing suspensions on a Buehler Trident polishing cloth. Samples were rinsed with Millipore water and dried under flowing argon gas.

1.5.4 Electron Backscatter Diffraction

Polished samples were analyzed with an environmental scanning electron microscope (FEI Quanta 600 F) outfitted with an electron backscatter diffraction (EBSD) detector (Oxford Instruments) to confirm crystallographic orientation after mounting and polishing.

1.5.5 Metal Coating

Embedded samples were secured to an aluminum stub with cyanoacrylate adhesive, coated with ~40 nm of Ni with an Ion Beam Sputter Deposition and Etching System (IBS/e, South Bay Technologies) operating at a base pressure below 10^{-4} Pa, a working pressure of 10^{-2} Pa Ar, with two ion guns operating at 8 kV and 3 mA per gun. The coating was grounded to the stub with conductive liquid silver paint.

1.5.6 APT Sample preparation

Samples for APT were prepared using the DualBeam scanning electron microscope (SEM) and focused ion beam (FIB) instrument (Helios NanoLab, FEI) using established protocols[46]. Briefly, the electron beam (5 kV, 1.4 nA) was used to locally decompose an organometallic precursor gas, methyl cyclopentadienyl trimethyl platinum [$C_5H_5Pt(CH_3)_3$], on the polished cross section to deposit a rectangular strap (2 x 25 μm) of platinum (FIB-Pt) over a region of interest. Subsequently, a protective rectangular cap of FIB-Pt was deposited over the same area using the ion beam (30 kV, 93 pA) to a final thickness of approximately 0.4 μm. A wedge of material below the protective FIB-Pt was cut out on three sides (30 kV, 6.5 nA). The wedge was attached to an *in situ* tungsten nanomanipulator (OmniProbe 200, Oxford Instruments) using FIB-Pt (30 kV, 93 pA) before cutting the final edge free (30 kV, 6.5 nA). 1-2μm wide segments were cut from the wedge (30 kV, 6.5 nA) and sequentially affixed with FIB-Pt (30 kV, 93 pA) to the tops of Si posts in an array (Cameca Scientific Instruments). Each tip was shaped and sharpened using annular milling patterns of increasingly smaller inner and outer diameters (30 kV, 9.3 nA). The majority of the amorphized surface region and implanted gallium in the tip surface was removed by cleaning (2 kV, 0.4 nA).

1.5.7 APT Methods

Atom probe tomographic analyses were conducted using a Cameca local-electrode atom-probe tomograph (LEAP 4000XSi, Cameca). Samples were analyzed using a pulsed frequency-tripled Nd:YAG laser (λ = 355 nm). Run time parameters (0.5 pJ, detection rate of 0.005 ions per laser pulse, pulse repetition rate 500 kHz and a base temperature of 35 K) were optimized for stoichiometry, signal to noise and spectral resolution while minimizing sample fraction as further described in Figure 1.3. The analysis chamber vacuum pressure was maintained below 10^{-8} Pa.

1.5.8 APT Reconstruction

3D Reconstructions of the APT dataset were performed using Cameca's integrated visualization and analysis software (IVAS) using standard algorithms and assuming a hemispherical tip shape[47,48]. The following reconstruction parameters were used: image compression factor ICF, ξ = 1.9, the evaporation field = 36 V nm^{-1}, detector efficiency variable = 0.486 and the field factor, k_f = 3.3. These were systematically determined in the following order. First, the radius of curvature determined the field evaporation factor after APT analysis. Secondly, the ICF was determined from previous work with homogeneous magnetite in [110] orientation, which exhibited two [111] poles. Thirdly, the field factor was held fixed at 3.3. Finally, the detector efficiency was augmented to optimize the angle between the platelets and their aspect ratio. In the titanomagnetite, exacting reconstruction parameters were employed.

1.5.9 Compositional Analysis

Compositional analysis was carried out using decomposition of peaks functionality in IVAS. Briefly, this software accepts user input elements and molecular fragments, along with their respective charge states. Subsequently, the algorithms attempt to fit each peak to the input list, taking into account expected isotope ratios. In the case of significant spectral overlap (TiO^{2+} and O_2^{+}) at 32 amu, the peak was manually partitioned.

A volumetric slice was stepped parallel to the surface normal through the interface between matrix and precipitate to determine compositional profiles. At each step, the compositions were averaged over the cylindrical (LP204-1, $r= r_{platelet} - 3$ nm, $h=w_{platelet}$ +20-30 nm) or cuboid (titanomagnetite, $a=a_{platelet} - 5$ nm, $b= b_{platelet} - 5$ nm, $c= c_{platelet} - 5$ nm) slices such that the high-curvature periphery of the precipitate was excluded from analysis. The step size was 0.5 nm and the step direction parallel to the shortest dimension of the slice. Concentrations are reported as atomic percentages within each volumetric slice.

1.5.10 Electron Backscatter Diffraction

Oriented, polished, uncoated cross sections were mounted onto an aluminum stub using carbon tape and analyzed with an environmental scanning electron microscope (Quanta ESEM, FEI) outfitted with an electron backscatter diffraction detector (Oxford instruments) to confirm crystallographic orientation after mounting and polishing processes. Integrated Oxford Aztec EBSD system (Oxford Instruments) was used in conjunction with custom software (Mathematica 9, Wolfram Research) to analyze electron backscatter diffraction data to find in plane direction relative lab axes.

1.5.11 TEM Sample Preparation

Transmission electron microscopy (TEM) samples were prepared from oriented, polished cross sections following established lift-out procedures with a DualBeam scanning electron microscope (SEM) and focused ion beam (FIB) instrument (Helios NanoLab, FEI).[49] Briefly, a 2 x 25 μm rectangular strap of platinum (FIB-Pt) was deposited perpendicular to the crystallographic direction of interest using the ion beam (30 kV, 93 pA). On either side of the strap, stepped-trenches were then milled out (30 kV, 6.5 nA), such to create a flat wall on opposing sides of the sample. This slice of material was cut free (30 kV, 2.8 nA) from the substrate on three sides leaving only small connecting bridge. An *in situ* tungsten nanomanipulator probe (OmniProbe 200, Oxford Instruments) was attached to the free side of the substrate using FIB-Pt (30 kV, 93 pA). The remaining bridge to the substrate was milled away (30 kV, 6.5 pA) and the probe was retracted with the sample. The sample was then welded to a copper TEM half-grid (Omniprobe) using

FIB-Pt, and the probe was cut free (30 kV, 93 pA). The thin sample was successively thinned to ~100 nm at 30 kV (93 pA) at a grazing angle (1-2º). To remove amorphized material and material implanted with Ga, the surface was cleaned with two successive low angle (~7º) milling steps at 5 kV (28 pA) and 2 kV (28 pA), thinning the sample to approximately 40-60 nm.

1.5.12 Bright Field Transmission Electron Microscopy

Conventional bright field TEM was performed with a Hitachi H-8100 TEM equipped with a tungsten hairpin filament operating at 200 kV. The TEM copper half-grid was loaded onto a low-background double tilt holder, to allow for tilting to zone axis. Images were integrated for 3 s to maximize sample to noise and limit beam damage.

1.5.13 High Angle Annular Dark Field Scanning Transmission Electron Microscopy

High angle annular dark field imaging (HAADF) was performed at 200 kV on a JEOL JEM-2100 FasTEM equipped with a high brightness Schottky FEG emitter source and a Gatan annular dark-field detector. Unless otherwise noted, images were collected with a pixel dwell time of 50 µs, a camera length of 2 cm and collection angle from 122.5-251.4 mrad.

2 AMORPHOUS INTERGRANULAR PHASE CONTROLS THE PROPERTIES OF HUMAN TOOTH ENAMEL

This section delves into the structure and chemistry of an amorphous intergranular phase in human enamel. This work was pioneered in mouse and various other rodent enamels, namely rat in the following seminal work:

> Gordon, L. M., Cohen, M. J., MacRenaris, K. Pasteris, J. D., Vine, D. J., Phatak, C., & Joester, D. Amorphous intergranular phases control the properties of tooth enamel. *submitted*. [referenced as "Gordon, *et al.*" in text]
>
> Gordon, L.M., Cohen, M.J., & Joester, D. Correlative Microscopy and Spectroscopy of Buried Interfaces in Tooth Enamel. Microscopy and Microanalysis 19, 1634-1635 (2013).

Lyle Gordon, Northwestern University (Pacific Northwestern National Laboratory) assisted with establishing atom-probe sample preparation and data analysis. His work is specifically noted in experiment design and X-ray spectroscopy data analysis. He, along with Dr. Tom Reiger, Canadian Light Source, assisted with X-ray spectroscopy. Parts of the work have been published in the above conference proceeding and are further in preparation as noted above, or will be published in future publications.

2.1 Introduction

Dental caries, commonly known as tooth decay, own an infamous designation as the most prevalent disease of the human race.[50,51] An acidic environment produced by a bacterial biofilm on teeth slowly dissolves the underlying enamel. This sequence can trigger extreme pain and potentially lead to gingivitis and periodontitis. Caries disrupts eating, speaking, and is known to be linked to systemic diseases such as pneumonia and atheromas.[50,52] With estimates of $104.8 billion in spending on dental care in 2010 in the United States alone,[51] this disease demands significant attention. In response, governmental agencies worldwide utilize systemic dosing of fluoride, via public drinking water as a preventative measure against tooth decay. Community water fluoridation (CWF) is touted as the premier public health effort, estimated to save an astounding $9.3 billion in caries related damages.[53] Systemic dosing is designed to increase the fluoridation of hydroxyapatite (HA), the hard bio-ceramic comprising the enamel of teeth. Fluoridation of hydroxyapatite decreases enamel's inherent susceptibility to acidic dissolution by carious attack.[50] Studies reveal a marked decrease in prevalence of dental caries since the adoption of CWF policies: 23% cavity decrease in twelve to seventeen year-olds from 1971 to 1991.[53] However, systemic dosage of fluoride is not fully understood. The efficacy and the science supporting systemic fluoride treatment continues to be ardently debated.[54] Specifically, it is unknown how fluoride is integrated into an adult's mature teeth upon exposure from drinking water and gel dentifrice (toothpaste).

The susceptibility of enamel to acid dissolution has long been shown to be dependent on the presence of not only fluoride ions, but also magnesium and carbonate [CO_2^{3-}] as well.[50] However, imaging the distribution of these impurities in enamel at the nanoscale level has remained a great challenge, hampering our understanding of caries etiology at a mechanistic level. Here we show by atom probe tomography that the majority of F in human enamel, when doused in a F^- containing solution (NaF), is located at intercrystalline, grain boundary localities. Further, through atom probe tomography, in concert with X-ray absorption spectroscopy, we show that the majority of Mg in human enamel is localized at the same grain boundary as a precipitate of Mg-substitute amorphous calcium phosphate. This finding echoes previously submitted work in murine enamel by Gordon, Cohen, MacRenaris, Pasteris, Vine, Phatak and Joester [henceforth, simply Gordon, *et al.*]. We also argue that these metastable, highly soluble precipitates are responsible for allowing the rapid and highly anisotropic acid etching of enamel and provide short circuit pathways for fluoride diffusion. The implication of these findings is the potential use of APT in medical research to assist the community in understanding biomineral related disease etiology. Further, grain boundary engineering in human enamel may be the next frontier for developing "post fluoride" dental care products.

Tooth enamel is a complex organic-inorganic hierarchical-nanostructure made up of bundled HA crystals paired with 2-5% fluid and protein.[55] Enamel crystals deviate from the theoretical HA stoichiometry [$Ca_{10}(PO_4)_6(OH)_2$] as a result of numerous ionic substitutions. Enamel is organized into an incredibly intricate hierarchical structure that provides superior toughness and wears resistance, far exceeding those of a synthetic apatite crystal. In fact, a homogeneous crystal of HA would quickly shatter under the forces typically seen during mastication. Enamel is comprised of long interwoven 2 to 5-micron diameter rods [Fig 2.1]. Each rod is comprised of thousands of aligned individual HA nanocrystals.[50] At the nanoscale, each crystal is partitioned by a typical grain boundary. At the macroscale, each rod is separated by disordered crystals, organics, other chemical substituents and small pores.[50] In concert, these elements construct a complex architecture.

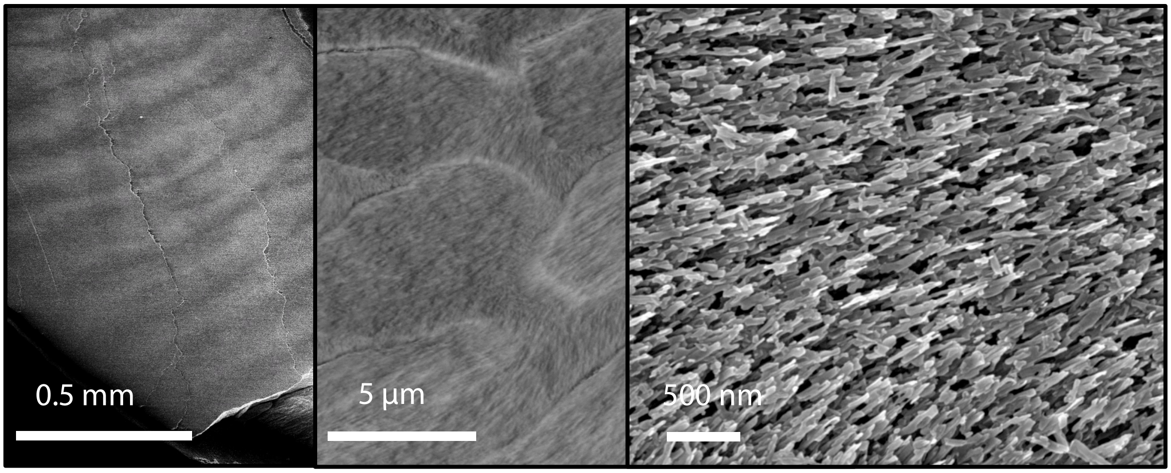

Figure 2.1 Hierarchical structure of human enamel (etched). Left: micron scale hunter-shrager bands of human enamel. Center: micron sized bundles of rods. Right: individual etched, high-aspect ratio, HA nanowhiskers

Presently, it is understood that at a macro- and microscopic level, fluoride is heavily concentrated at the tooth surface within the first 13.5 microns.[56] This work is commonly determined through analysis of ground enamel to probe diffusion and incorporation.[50,57] The reader can quickly see how work in powdered enamel ignores the critical microstructure described above [Fig 2.1]. Researchers posit that fluoride localizes either at structural defects within the hierarchical structure, in non-apatitic fluorine rich phases (such as fluorite, CaF_2) or on the tooth surface.[50] Unfortunately no strong supportive evidence seem to bolster any of these propositions because the utilized techniques can't resolve chemical topography at the nanometer scale,[57] blind to the intricate nanostructure of enamel. It is crucial to realize where fluoride is located because it will allow us to truly understand the mechanism of protection from acid corrosion. It is thought that acid permeates enamel at the grain boundaries, as that is the most susceptible portion. We must know for certain where diffusion of ions and acidic fluid is occurring through the structure. By completely understanding the mechanism for transport and corrosion in teeth, we can take the next step to improving preventive care.

2.2 Results and Discussion

The susceptibility of enamel to dissolution in acidic environments was qualitatively evaluated by acid etching, a technique commonly used to reveal micro- and nano-structure of mineralized tissues.[58] These etching conditions are designed to roughly approximate intra-oral conditions that occur during carious attack. Enamel was subjected to lactic acid, and within 15 s, we observe rapid preferential etching at intra-rod locations [Fig 2.2b] relative to a polished cross section [Fig 2.2a]. Note that the polished cross section (polished in the presence of water), displays subtle etching, as expected, but the etching seems to be at the intra-bundle locations. This observation is commonly seen through the literature, causing many to theorize that there are chemical distinctions in the intra-rod space.

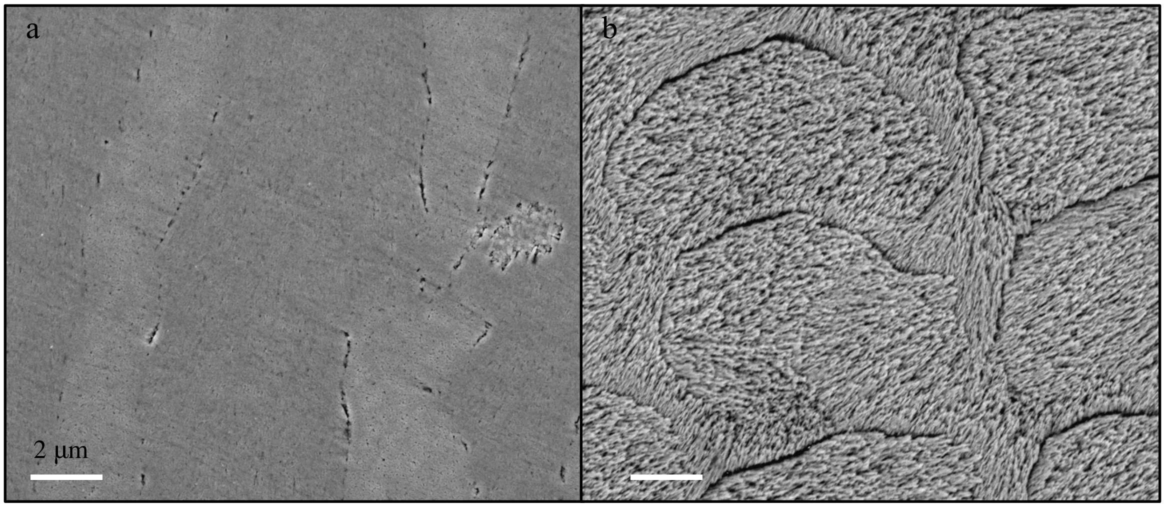

Figure 2.2| scale bars are both 2 µm; a| Polished human enamel surface; b| human enamel post-15 s of lactic acid etch.

Enamel is a chemically heterogeneous material with numerous trace impurities, which can be difficult to detect with conventional microscopy and spectroscopy tools due to the technique's inherent sensitivity-variation across the periodic table. Since these dilute impurities (e.g. F^-, Cl^-, Mg^{2+}, CO_2^{3-}, Na^+) have a tremendous impact on the chemistry and solubility relative to acid, the need to analyze the quantity and position of these ions is imperative. We utilized atom-probe tomography (APT), a microscopy technique that is uniquely capable of elucidating the nanoscale structural and chemical complexity of biological minerals, including bone and dentin,[3] which are compositionally analogous to the mineral phase in tooth enamel. Optimizations of APT run-time parameters are outlined in Fig 2.3. The background exhibits an exponential decay as laser power increases [Fig 2.3a]. This is to be expected, as higher laser powers require lower operating voltage to reach steady evaporation rates. Operating laser power was chosen to optimize tip throughput (decrease fracture) and concentration of Ca, O and P. The chosen laser powers were 50 pJ and 75 pJ. This range of laser levels balances both a low

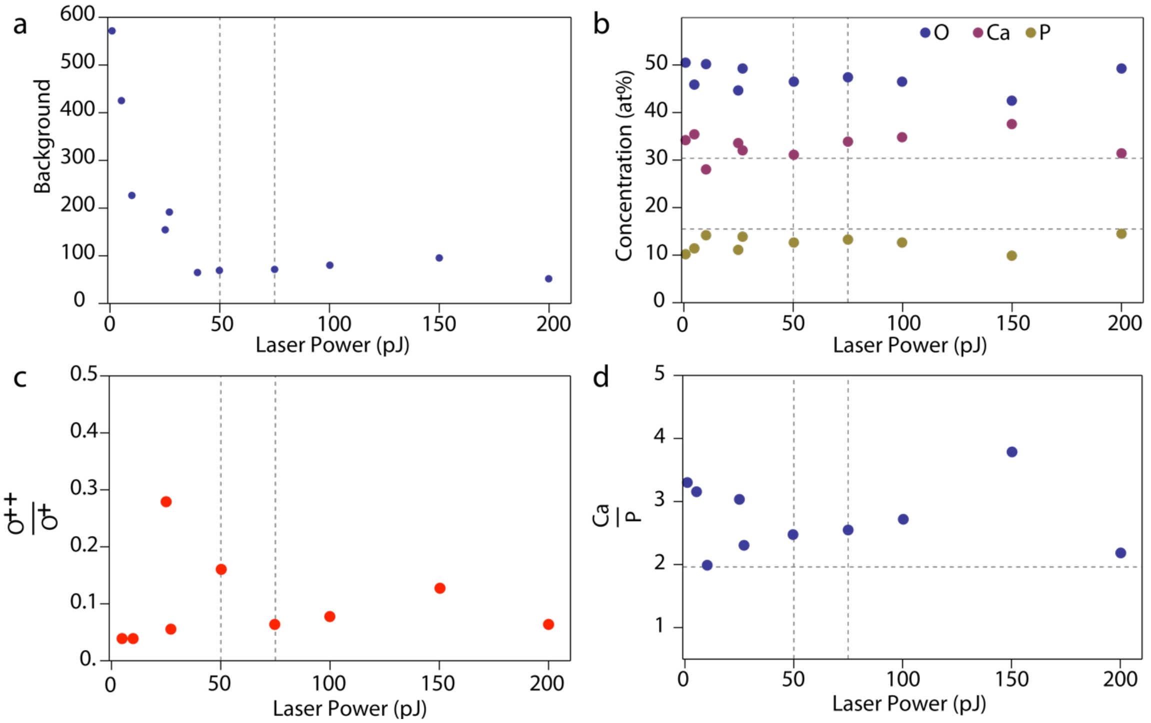

Figure 2.3| Variation of APT parameters; a| Background versus laser power shows normal decay; b| concentrations of main elements [O, Ca, P] versus laser power; c| Ratio of O2+2/O2+ versus laser power, comparing the balance of oxygen at 16 versus 32 amu; d| Ca/P ratio, a commonly reported ratio for HA

background, but shows accurate Ca/P ratios. The 200 pJ setting seems to be a general outlier.

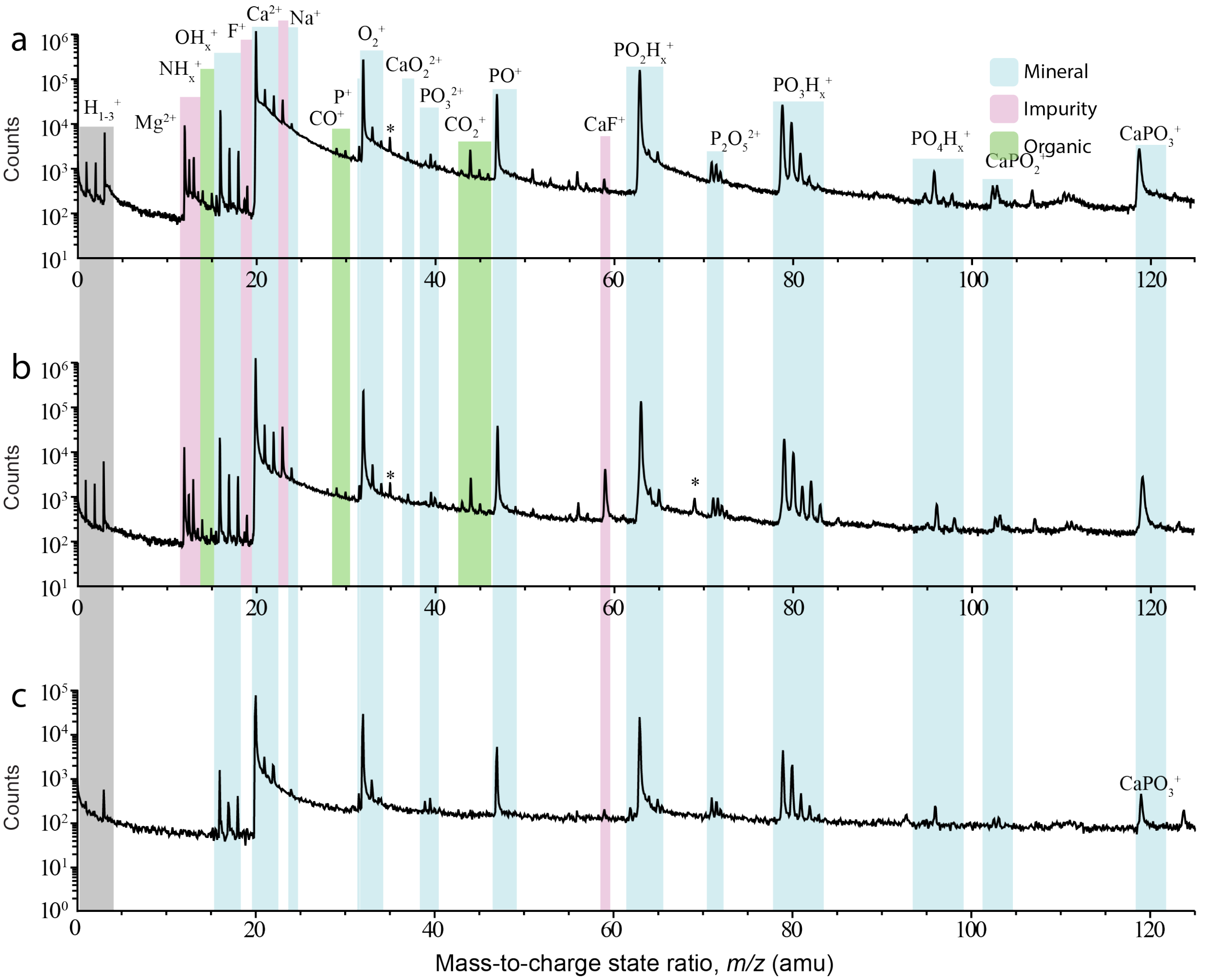

Figure 2.4| a| Mass to Charge spectra for Human enamel; b| spectra for Fluoride doped-Human enamel; c| spectra for synthetic HA.[3] * denotes contributions from FIB ^{69}Ga

APT mass to charge ratio spectra [Fig 2.4] obtained from third molar outer and fluoride-treated enamel consisted primarily of Ca, P and O containing atomic and molecular ions, consistent with synthetic hydroxylapatite. In addition, Mg, Na, Cl, F, C and N (organic) containing ions were identified. However, these peaks were not seen in the synthetic HA [Fig 2.4c]. Ca^{2+} is the dominant mineral peak, but other Ca containing fragments are identified ($CaPO_3^+$). Mg is found similarly at the divalent peak, but the 1+ form is seen as well (yet overlaps with a $^{44}Ca^{2+}$). P is almost completely found in oxygen-, hydrogen-, or calcium-containing molecular fragments, but P^+ is resolved as a small peak, or shoulder to the left of O_2^+. In the fluoridated human enamel, we see an increase in contribution from the F^+ peak at 19 amu, but the dominant peak is CaF^+ at 59, which is barely seen in the non-fluoridated human enamel. The synthetic hydroxyapatite sample shows similar mineral contributions, but as expected lacks most impurity peaks. However, the appearance of CaF^+ in this standard is seen. For full analysis of identified peaks see Table 2.1.

m/z (AMU)	Chemical Identity		m/z (AMU)	Chemical Identity
1, 2, 3	H^{1+}, H^{2+}, H^{3+}		34.5	Ga^{2+}
12, 12.5, 13	$^{24,25,26}Mg^{2+}$		36	CaO_2^{2+}
14	N^+		39.5	PO_3^+
15	NH^+		44	CO_2^+
16, 17, 18	$^{16}OH_x^+$, ^{18}O		47	PO^+
19	F^+		59	CaF^+
20, 21, 21.5, 22, 23, 24	$^{40,42,43,44,46}Ca^{2+}$		63, 64, 65	$PO_2H_x^+$
23	Na^+		69	Ga^+
24	Mg^+		71, 71.5	$P_2O_5H_x^+$
28	CO^+		79, 80, 81, 82	$PO_3H_x^+$
31	P^+		95, 96, 97, 98	$PO_4H_x^+$
32, 33, 34	$O_2H_x^+$		103, 119	$CaPO_2^+$, $CaPO_3^+$

Table 2.1 List of major peaks identified in human enamel spectra.

The bulk concentration for the human enamel, without added fluoride is compared to the fluoridated sample in Table 2.2.

Element (at %)	Human Enamel (50 pJ)	F-Human Enamel (75 pJ)
O	50.39	50.30
Ca	31.52	28.51
P	14.23	15.5
H	2.40	2.36
Na	0.75	0.11
Mg	0.32	0.31
C	0.18	0.31
Cl	0.10	0.23
F	706 ppm	0.92
N	117 ppm	124 ppm

Table 2.2 Comparison of APT compositions: human enamel and F-doped human enamel.

There is a slight variation in composition between the two samples Ca and P, but with error and variation in laser power (50 pJ and 75 pJ respectively) between the human enamel and doped sample, they are essentially equal. As expected there is a marked increase of F. Over a 10 fold increase in the amount of detected fluoride in the bulk of the human enamel tooth. This is to be expected, as the F diffused into the material. Other trace elements are roughly consistent, although Na decreases noticeably in concentration, but this could be due to the increase in F and P at% in the fluoridated sample, or due to local sample variations.

Three-dimensional reconstruction of the human fluoride-doped enamel samples, rendering Mg ions detected [Fig 2.5a], showed a distinct intergranualar-phase, rich in F and Mg [Fig 2.5a,b]. The bulk of the enamel crystals remained somewhat free of Mg substituent elements, but seems to contain a higher quantity than observed in mouse enamel by Gordon, *et al*. Reconstructions, while not exactly spatially precise, suggest that the grains are roughly ~20 nm in width, in agreement TEM[59] and SEM measurements. However, the grain boundaries become much more apparent when we render all detected F atoms. Since the amount of F in the non-doped human enamel is near negligible, we can observe that the incoming F diffuses into the grain boundaries through probable short-circuit diffusion. By creating an iso-density surface for the Mg atoms of 0.2 nm^{-3}, we can isolate the grain boundaries of the sample. Analyzing the concentrations of the grain boundaries [Table 2.3] versus the crystals shows the increase in Mg and F, and suggests a potential solubility limit for Mg.

Element (at %)	Grain Boundary (> 0.2 Mg/nm^3)	Crystal (< 0.2 Mg/nm^3)
O	47.73	50.78
Ca	31.82	27.86
P	14.83	15.67
H	1.62	1.05
Na	1.31	1.05
Mg	0.58	0.31
C	0.29	0.31
Cl	0.19	0.24
F	1.40	0.82
N	151 ppm	118 ppm

Table 2.3 Comparison of APT compositions: F-doped human enamel grain boundary region and the bulk of the crystal.

This shows how strongly F and Mg partition into the grain boundary (and to a lesser extent organics, resolved as N). The partition coefficient, log $P_{\text{gb/crystal}}$ = … 0.53 for F; 0.63 for Mg; and 0.25 for N. This suggests a solubility of Mg in the bulk of HA is perhaps 0.35-0.5 at%, as Mg above this cut-off is excluded to the periphery of the nanowhisker. The slight increase in N also supports previous observations that most organic lies outside of the HA crystal, and is perhaps not incorporated into the HA crystal itself. Proxygrams are also useful to resolve this partitioning across the grain boundary in real space. Here we see the increase of Mg across the grain boundary, with a gradient over about 2.5 nm. The F shows a slightly shorter gradient, but the matrix concentration is higher for F. [Fig 2.5 e,f]

Literature estimates the solubility of 0.3 at% Mg in HA.[60,61] Others have proposed synthetic fabrication of higher Mg content, but have not truly proven the incorporation of Mg into the crystal lattice with NMR, XAS or other techniques capable of proving incorporation.[62] This supports our conclusions that the Mg is perhaps mostly located within the grain boundaries. In mouse enamel, we found that the bulk composition of Mg was around 0.13 at%, much lower than found in Human enamel. This suggests that human enamel incorporates a greater fraction of Mg within the crystal relative to the grain boundary. However, we still see a large amount of Mg (0.58 at%) located in what appears to be grain boundaries. This suggest that the high amount of Mg could be incorporated into a different phase, as found in Mouse enamel. In mouse enamel, X-ray absorption was successfully utilized to prove that the intergranular phase was a Mg-doped amorphous calcium phosphate (Mg-ACP).

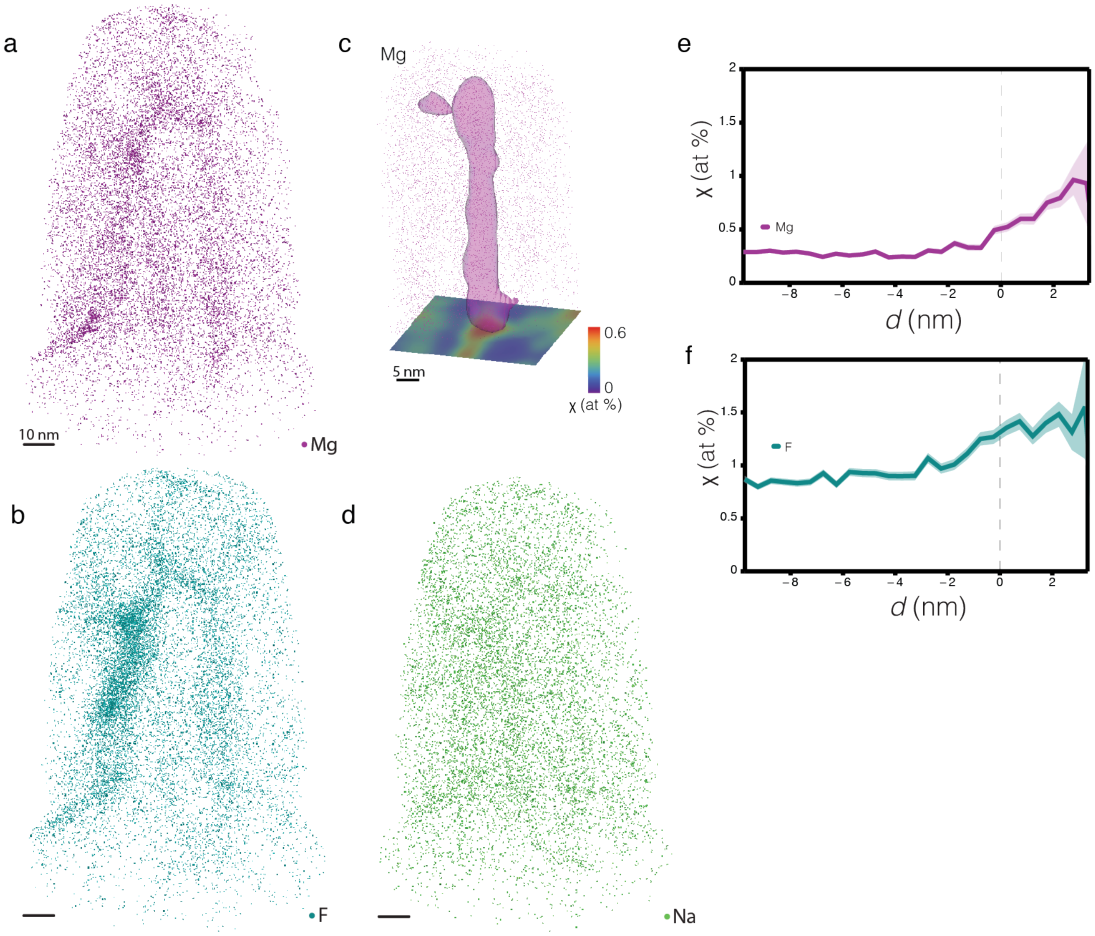

Figure 2.5| a| APT reconstruction of just Mg; b|: Reconstruction of all F; c| Isosurface of 0.2 Mg/nm^3 with Mg-concentration map underlying; d|: APT reconstruction of Na; e| and f| Proxygram showing increase of Mg and F across grain boundary, respectively. All from NaF-doped human enamel.

Here, we shall consider similar high-Mg non-apatitic phases as potential crystalline incorporators of Mg, such as dolomite, huntite or whiltockite. These are posited as potential minority constituents in human enamel.[61,63] X-ray absorption spectroscopy (XAS) proves to be an excellent correlative technique in conjunction with atom probe tomography. While X-ray diffraction is limited to probing long-range ordered crystalline materials, XAS is remarkably sensitive to local environment around a specific atom.[64] Since we have shown a notable accumulation of Mg within specific locations of the sample, we can use k-edge Mg XAS to probe Mg located within the Mg-rich space, while working in bulk. Here we are considering huntite [$Mg_3Ca(CO_3)_4$], dolomite[$CaMg(CO_3)_2$] and whitlockite [$Mg(PO_4)PO_3OH$] which are compositionally similar to enamel but have not been observed *in vivo* experimentally inside enamel.[61]

Near the Mg-edge at 1305 eV, we see strong peaks in the crystalline samples as discussed by Gordon, *et al.* These near-edge peaks are strongly suggestive of crystallinity and are associated with first-coordination electronic transitions and multiple scattering from higher shells [Fig 2.6 left].[65] As discussed by Gordon, *et al.*, the Mg-ACP and Mouse Enamel show almost no multiple scattering events, which shows that the fluorescence detected is dominated by the first shell and beyond that, material is lacking long-range order. In the Human enamel, we see a similar broad feature as we do in the Mg-ACP and Mouse enamel. However we doo see a sharper peak at 1312 eV, suggestive of multiple scattering events beyond the first shell. This could be a result of the much higher bulk Mg content that we find from the APT, suggesting that the 0.32 at% Mg within the bulk is participating in long-range ordered crystals and contributing to this peak we see in XANES.

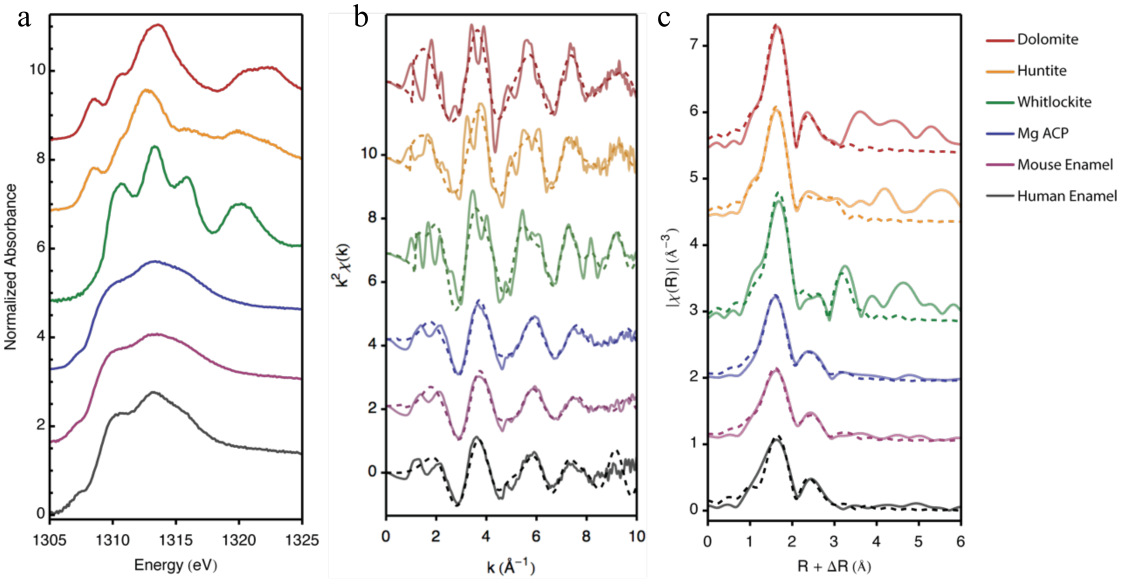

Figure 2.6| Mg *K*-edge X-ray absorption spectroscopy [reference spectra from Gordon, *et al.* X-ray absorption spectra for dolomite, huntite, whitlockite, Mg doped ACP, mouse enamel and human enamel. a| XANES; b| space (k^2 weighted) EXAFS; c| real space EXAFS. Fits (dashed lines) are displayed with measured EXAFS data (solid lines).

This qualitative description rooted in XANES is supported by the EXAFS spectra. It is quickly observed that the Mg-ACP, Mouse Enamel and Human enamel EXAFS spectrum are all quite distinct from the crystalline reference materials. These lack high frequency components around 4 k. However, at 4.8 k, we see a strengthened peak relative to Mg-ACP and Mouse Enamel in the Human enamel spectra. Quantitative analysis of the local bonding environment of the Mg atoms was conducted, as by Gordon, *et al.* by fitting the spectra with theoretical scattering paths. ACP and Enamel spectra were fit to HA structure, as the structure and thus scattering paths of an ACP material is unknown and variant.

In Human enamel, we find similar features to Mouse Enamel and Mg-ACP, but different measured bond lengths. From previous work (Gordon, *et al.*) we found a short Mg-O bond (2.03 Å), matching that found in Mg-ACP (2.02 Å) [Table 2.4]. However, in Human enamel, the fitted Mg-O bond is 2.09 Å. This is much longer than found in ACP or Mouse Enamel, and much closer to that found in Whitlockite. This suggests that either the fit is poor due to low data quality, that the larger amount of Mg in the bulk (relative to murine enamel) is participating in more crystalline like bonding, or that the sample damaged during scanning. The final explanation is eliminated by multiple scans in different locations within the powdered sample exhibiting similar spectra. Performing additional scans with Human enamel, perhaps from different teeth could eliminate the first argument. Finally, the middle explanation could in fact be real. In Mouse Enamel, we find 0.07 at% Mg in the bulk, while in Human enamel, here we report 0.31 at%. This increase in bulk Mg, while still below suggested solubility limits, could explain the increase in crystalline-like character.

Sample	Path	R (Å)	CN	σ^2	ΔE (eV)	R-factor
Dolomite	Mg-O$_1$	2.07(1)	6*	0.0038(9)	4.4	0.7%
	Mg-C	2.99(3)	6*	0.001(3)		
	Mg-O-C	3.14(6)	12*	0.005		
	Mg-O$_2$	3.48(4)	6*	0.010(8)		
Huntite	Mg-O$_1$	2.06(1)	6*	0.006(1)	3.5	1.2%
	Mg-C	3.08(8)	6*	0.01(2)		
	Mg-O-C	3.4(2)	12*	0.02		
	Mg-O$_2$	3.38(4)	6*	0.01(1)		
Whitlockite	Mg-O	2.08(2)	6*	0.006(2)	5.3	5.5%
	Mg-P	3.37(6)	6*	0.006(7)		
	Mg-Ca	3.50(4)	6*	0.004(4)		
Mg-ACP	Mg-O	2.02(2)	3.8(8)	0.005(3)	1.8	1.3%
	Mg-P$_1$	3.17(6)	3(3)	0.005(9)		
	Mg-P$_2$	3.39(8)	3(3)	0.005(9)		
Mouse Enamel	Mg-O	2.03(2)	4(1)	0.00899	0.9	1.0%
	Mg-P$_1$	3.18(6)	3(3)	0.003(9)		
	Mg-P$_2$	3.40(9)	3(3)	0.003(9)		
Human Enamel	Mg-O	2.09(2)	4†	0.006(3)	-10.9	3.3%
	Mg-P$_1$	3.08(8)	3†	0.003(8)		
	Mg-P$_2$	3.28(7)	3†	0.003(8)		

Table 2.4 EXAFS shell-by shell fitting. Reference data and table from Gordon, *et al.* Radius, coordination number, and σ^2 shown for each fitted scattering path. *ΔE* is fixed for each individual paths but varies between samples, while the amplitude reduction factor was found previously (Gordon, *et al.*) to be (0.8) by fitting the reference spectra (dolomite, huntite, whitlockite). Bold coordination values were held constant. Uncertainty in parenthesis for last digit. *designates a CN from crystal structures. †designates CN fixed based on previous work with mouse enamel to improve fit.

2.3 Conclusion

Here we report a continuation of Gordon, *et al.* by considering human enamel, and comparing it to murine enamel. In that work, we found, through APT analysis of mouse enamel, that there exists a Mg-rich grain boundary in mouse enamel. Evidence from *ex vivo* etching experiments shows preferential etching down grain boundaries, which reinforces the hypothesis of chemical differences at the grain boundaries. Work by others[59] in human enamel supports this conclusion. In APT experiments with human enamel, we find a enrichment of above the solubility limit within the grain boundaries, although we still find appreciable Mg within the bulk of the HA nanowire. This suggests that human enamel may incorporate more Mg into the crystal than mouse enamel. XANES and EXAFS agree with this finding, showing great multi-scattering events and longer Mg-O bonding, suggestive of some long-range order. However, the XANES and EXAFS still support the claim that the majority of the Mg found in human enamel is located within an amorphous film. By adding dissolved fluoride to the system, APT shows a colocalization of F with the Mg-rich grain boundaries. This is in agreement with Gordon, *et al.* where quantified etching experiments suggest that topical fluoride treatment of rabbit teeth decreases enamel susceptibility to mineral loss during acidic attack. This work highlights not only the promise of APT as a technique for understanding medically relevant problems, but also in helping to better understand prophylaxis.

2.4 Materials and Methods

[modified from Gordon, Cohen, *et al.*]

2.4.1 Consumables

Unless otherwise specified, the following chemicals were used without further purification: potassium hydroxide (KOH), sodium hydroxide (NaOH), acetone [$(CH_3)_2CO$] (VWR, West Chester, PA); bromo-form ($CHBr_3$), sodium fluoride (NaF), calcium nitrate tetrahydrate [$Ca(NO_3)_2 \cdot 4H_2O$], magnesium nitrate hexahydrate

[$Mg(NO_3)_2 \cdot 6H2O$], ammonium phosphate dibasic [$(NH_4)2HPO_4$], sodium phosphate (Na_3PO_4), lactic acid ($C_3H_6O_3$), magnesium oxide (MgO) (Sigma-Aldrich, St. Louis, MO); Epo-Tek 301 epoxy (Epoxy Tech-nology, Billerica, MA); CarbiMet II SiC grinding paper, Microcut SiC grinding paper, Metadi supreme polycrystalline aqueous diamond polishing suspension, Masterprep Alumina suspension, Trident polishing cloth, Chemomet polishing cloth (Buehler, Lake Bluff, IL); Conductive Liquid Silver Paint (Ted Pella, Redding, CA). Super Glue Cyanoacrylate Adhesive (3M, St. Paul, MN); Ultrapure Water (ρ=18.2 MΩ·cm) was prepared with a Barnstead Nanopure UF+UV ultrapure water purification system (Thermo-Fisher Scientific, Waltham, MA).

2.4.2 Embedding, Grinding and Polishing

De-identified human third molars were obtained from an anonymous dentist. Molars were diced along the labiolingual plane using a bone saw incisors and subsequently dried in air. Slices were embedded in Epo-Tek 301 epoxy and polymerized overnight at 25 °C. Embedded samples were ground using progressively finer grits of Buehler SiC grinding paper (400, 600, 800 & 1200 grit). Ground samples were polished using 3 µm and 1.0 µm polycrystalline aqueous diamond polishing suspensions on a Buehler Trident polishing cloth. After a final polishing step using 0.05 µm Al_2O_3 suspension on a Buehler Chemomet polishing cloth, samples were rinsed with water and dried under flowing argon gas.

2.4.3 Fluoride Exposure

Freshly ground and polished human molar cross-sections were submerged in 250 mM aqueous NaF solution and maintained at 37 °C for 24 hr on a rotator. Following fluoride exposure, samples were rinsed with water and dried under flowing argon gas.

2.4.4 Mounting and Coating

For SEM imaging, samples were secured to an aluminum stub with cyanoacrylate adhesive, coated with ~5 nm of Pt with an Ion Beam Sputter Deposition and Etching System (IBS/e, South Bay Technologies, San Clemente, CA) operating at a base pressure of $< 10^{-4}$ Pa and working pressure of 10^{-2} Pa Ar, with two ion guns operating at 8 kV and 3 mA per gun. The coating was grounded to the stub with conductive liquid silver paint.

2.4.5 Scanning Electron Microscopy

SEM was performed with an FEI Helios Nanolab (Hillsboro, OR) operating at 5 keV with 0.4 nA probe current.

2.4.6 Atom Probe Tomography Sample Preparation

Samples for APT were prepared using the dual-beam SEM/FIB instrument (Helios Nanolab, FEI, Hillsboro, Oregon) using established protocols.[66] A rectangular strap of platinum (FIB-Pt) was deposited over a region of interest on the polished cross-section using the ion beam (30kV, 93pA) to locally decompose an organometallic precursor gas, (trimethyl)methylcyclopentadienyl-platinum $(CH_3)_3Pt(CpCH3)$, over a region of interest (2 x 25 μm) on a polished cross-section. A wedge of material below the Pt strap was cut out on three sides. The wedge was attached to an in-situ nano-manipulator (Omniprobe, Dallas, TX) using FIB-Pt before cutting the final edge free. 1-2μm wide segments were cut from the wedge and sequentially affixed to the tops of Si posts in an array (Cameca Scientific Instruments, Madison, WI) with FIB-Pt. Each tip was shaped and sharpened using annular milling patterns of increasingly smaller inner and outer diameters. The majority of the amorphized surface region and implanted gallium in the tip surface was removed by milling at 2 kV, 0.4 nA.

2.4.7 Atom Probe Tomography

Atom probe tomographic analyses were conducted in a Cameca local-electrode atom-probe tomograph (LEAP 4000XSi, Cameca, Madison, WI) using a pulsed laser (λ = 355 nm, 200-250 kHz, 50-75 pJ per pulse). The DC potential on a microtip during APT was controlled to maintain an evaporation rate 0.005 ions per laser pulse. The base temperature of the microtip was maintained at 25 K and the ambient vacuum pressure was below 10^{-8} Pa.

2.4.8 Spectral Analysis

For visualization and analysis, peak integration intervals were defined manually for all elements and molecular fragments. These definitions are used to create the 3D reconstruction in Cameca's integrated visualization and analysis software (IVAS).

Compositional analysis was carried out using decomposition of peaks functionality in IVAS. Briefly, this software matches isotope ratios to the list of potentially input elements and molecular fragments, which the user provides.

2.4.9 Reconstruction Analysis

Three-dimensional reconstruction of APT data was performed using the Cameca integrated visualization and analysis software (IVAS) based on published algorithms, assuming a hemispherical tip shape.[67,68] Standard reconstruction parameters were used with an electric field-dependent tip radius (*r*). The average evaporation field (F_e) of the enamel apatite ($14\ V\cdot nm^{-1}$) was used and determined previously [Gordon, *et al.*]. Atomic volumes for the reconstruction were calculated based on the hydroxyapatite crystal structure.

2.4.10 Reference Materials

Mg substituted ACP was prepared by rapidly mixing an 100 mL of an aqueous solution of Na_3PO_4 (0.20 M) by rapidly mixing with 100 mL of an aquous solution of $Ca(NO_3)_2$ (0.29 M) and $Mg(NO_3)_2$ (0.12 M) at 25°C. The resulting precipitate was immediately vacuum filtered, washed with water and dried under vacuum. The as synthesized Mg-ACC was determined to have an Mg/Ca ratio of 0.3 (6 wt% Mg) by ICP-MS.

Whitlockite was prepared based on Fadeev *et. al.*[69] Briefly, an aqueous solution of 100 mL $Ca(NO_3)_2$ (1 M)and $Mg(NO_3)_2$ (1.11 M) was stirred while 100 mL of an aqueous solution of $(NH_4)_2HPO_4$ (0.67 M) was added dropwise. The mixture was stirred for 4 hours and the resulting mixture was vacuum filtered, washed with water, and dried overnight at 100 $^{\circ}$C in air. The dried powder was subsequently heated to 700 $^{\circ}$C for 3 hours in air. The as synthesized whitlockite was determined to have an Mg/Ca ratio of 0.075 (1.6 wt% Mg) by ICP-MS.

High-purity synthetic hydroxylapatite was purchased from Sigma-Aldrich, product number 57479, purity ≥ 99.995% (trace metal basis). Certificate of analysis indicated 3 ppm Mg determined by atomic absorption mass spectrometry. Magnetite was purchased from Alfa Aesar and amorphous iron (III) phosphate dihydrate was purchased from Sigma-Aldrich.

Phase and chemical purity of reference materials was verified by powder X-ray diffraction (XRD) and inductively coupled plasma mass-spectroscopy (ICP-MS).

2.4.11 Powder X-ray diffraction

Powdered samples were suspended in acetone and dispersed on the surface of an off-axis cut quartz single crystal plate (MTI Technologies, Richmond, CA). Remaining acetone was allowed to evaporate. Samples were analyzed with a Scintag diffractometer with a X-ray source operating at 40 kV and 20 mA equipped with a Cu anode. Diffracted intensity was recorded between $2\theta = 5°–90°$ with a step size of 0.05° and a dwell time of 2 seconds per step. An energy dispersive X-ray detector was used to count only diffracted Cu-$K\alpha$ X-rays and exclude X-ray fluorescence.

2.4.11 Magnesium K-edge XAS

XAS measurements were performed at the Spherical Grating Monochromator (SGM, 11ID-1) beamline of the Canadian Light Source in Saskatoon, SK. Dry samples were prepared by spreading a small amount of powder on graphite tape (Ted Pella). Samples were scanned relative to the edge Mg *K*-edge (1303 eV) from -60 to -12 eV in steps of 2 eV; -12 to -8 eV in steps of 0.5 eV; -8 to 30 eV in steps of 0.1 eV; 30 to 190 eV in steps of 0.2 eV; 190 to 300 eV in steps of 0.3 eV; and 300 to 400 eV in steps of 0.5 eV with a constant dwell time of 2 seconds/step. Monochrometer energy calibration was performed by setting the first absorbance maxima of the MgO reference sample spectra to 1309.5 eV. X-ray fluorescence intensity was measured simultaneously with four solid state silicon drift energy dispersive X-ray detectors (Amptek, Bedford, MA). Incident flux was measured by recoding the current from a gold mesh upstream. The Mg X-ray fluorescence intensity was isolated from the total fluorescence intensity containing contributions from X-ray fluorescence from other elements and the scattered incident beam using custom written code in Mathematica (Wolfram Research, Champaign, IL). The exit slit was adjusted and the undulated detuned to reduce flux to prevent saturation of X-ray fluorescence detectors when measuring concentrated samples. Between 1 and 7 scans were collected for each sample and averaged. No beam-induced changes were observed when comparing sequential spectra.

2.4.11 Magnesium Extended X-ray Absorption Fluorescent Spectroscopy

The absorption data were normalized, background subtracted using AUTOBK, and converted to k-space using Athena.[70] Edge energy (E_0) was set to the maximum of the first derivative of the absorption spectra. $\chi(k)$ data were weighted by k^2 and Fourier transformed over the k range 2-9.5 Å^{-1} applying a Hanning window with a sill width of 1 Å^{-1}. Theoretical photoelectron scatting amplitudes and phase shifts based on the crystal structures of dolomite,[71] huntite,[72] whitlockite,[73] and hydroxyapatite[74] were calculated using FEFF6.[75] Shell-by-shell fitting of the EXAFS data was performed in *R*-space using

Artemis.[70] An energy shift parameter (E_0) was maintained constant for the scattering paths but allowed to vary between samples. The amplitude reduction factor ($S_0^2 = 0.8$) was determined based on a fit to the dolomite, huntite and whitlockite spectra with coordination numbers constrained based on their respective crystal structures. Multiple scattering in the carbonate reference samples was accounted for following Reeder *et. al*.[76] Enamel and ACP EXAFS were fit using a model based on the Ca[II] site of hydroxlapatite, consisting of a single Mg-O and two Mg-P scattering paths.[77,78] To minimize the number of fitting parameters the coordination number and σ^2 for the two Mg-P paths were constrained for each sample but allowed to float between samples.

3 INORGANIC-ORGANIC-INORGANIC DOUBLE-HYBRID INTERFACES IN CUPRITE NANOROD-GOLD NANOPARTICLE COMPOSITES

This section details a collaborative effort in understanding a construct created to model complex hybrid interfaces between organic and inorganic materials. Emily Asenath-Smith, Amanda Mae Uhl and Lara Estroff (Cornell University) conducted nanorod fabrication as well as TEM tomography experiments. Nanorod fabrication methods have been previously submitted as a Senior Thesis by Amanda Mae Uhl and edited here for reference. Her work as well as Emily Asenath-Smith's effort in perfecting and detailing the methods of fabrication and capturing TEM images is recognized. Parts of this work may be published in future publications or conference proceedings.

3.1 Introduction

Cuprous oxide [cuprite, Cu_2O] remains an intriguing material for its potential applications in solar energy conversion,[79] sensors,[80] photoelectrochemistry,[81] and other electronic materials).[82] With a direct band gap of 2.17 eV,[83] cuprite has intrigue in electronic material applications due to its high-intensity photoexcitation (~150 meV),[84] which makes it especially attractive in solar energy conversion. This material is also considered environmentally-friendly because it is inexpensive, nontoxic and a naturally abundant oxide.[81] While considerable efforts have been made in creating thin film-based constructs, such as the use of elevated temperatures to oxidize metallic copper,[85] reactive magnetron sputtering,[86] and electrodeposition;[87] creation of 1D cuprous oxide nanostructures remains particularly elusive. Nanorods of Cu_2O are especially useful in furthering the community's understanding of these oxides, specifically in experimentation with the concept of nanoscale confinement of excitons. It has been proposed that in 1D cuprite, excitons could flow in a coherent wave along the axial direction of a nanotube.[82] For these reasons, many groups[81,82,88,89] have studied the properties of Cu_2O single crystal nanostructures. Techniques ranging from solution-based processes to vapor-phase epitaxial growth have been employed, all while remaining hopeful to create 1D, single-crystalline nanostructures in order to facilitate the use of cuprous oxide nanowires as a building block for electronic devices. However, it remains challenging to create 1D, single crystalline nanostructures out of materials with a primitive cubic crystal structure such as cuprite.[82] Previous attempts to fabricate nanowires out of these types of materials have resulted in polycrystalline and tangled nanowires with unappetizing aspect ratios. The use of strategic confinement has been executed successfully. For example, Tan *et al.* created a core/sheath polymer-based structure in order to create single crystal nanowires.[82] While this path is fruitful in building nanowires, it limits ones ability to modulate electronic properties through creating composite materials decorated with nanoparticles.

Herein, we describe the fabrication and characterization of cuprite nanowires using external 1D-confined template strategies. This manufacturing technique allows us to create highly engineered single crystals with the incorporation of foreign materials to tailor properties. This type of construct is reminiscent of biominerals such as chiton teeth[90] and sea urchin embryo skeletons.[91] Previous work with chiton teeth,[90] and other biominerals reveals their remarkable ability to incorporate protein networks within a single, oxide crystals. The use of novel characterization techniques such as Atom Probe Tomography (APT),[90] HAADF[90] and TEM tomography[92] have shown to be excellent means of resolving the internal structure, and in the case of APT, the chemistry at the organic-inorganic interface between the biomineral and the organic materials within.[90]

We describe a cuprous oxide model system, not only for complex biomineralization and inclusion of foreign organics, but also to create a cuprous oxide-based construct for electronic-related fields. The system is comprised of Cu_2O Nanorods (Cu-NR), fabricated with Au-nanoparticles (Au-NP) stabilized by citrate [$C_6H_5O_7^{3-}$]. This construct is designed to mimic biogenic materials where occluded organic components can be found within single crystals for added structural, chemical biological properties[93] in confinement. Efforts in created oxide confined systems span polymeric templates,[82] colloidal crystals and track-etched membranes. Previous successes with semi-conducting metal oxides, such as zinc oxide [ZnO] and copper (II) oxide [CuO] in non-idiomorphic forms such as high-aspect ratio single crystals in track-etched membranes have been shown previously.[94] Further, success has been demonstrated of incorporating a secondary phase in both zinc oxide and cuprous oxide, without disrupting long range order in non-1D constructs.[95,96]

The characterization of cuprite nanorods, with widths on the order of 50-100 nm and lengths up to 1-3 μm is the focus of this chapter. By using track-etched membranes, not only as a means of confinement, but also as a means of dispersing Au-NP coated with citrate *in situ* for subsequent cuprous oxide growth. Gold nanoparticles serve many purposes, both as a mimic of included foreign entities but as a register of successful inclusion due to Au-NP ease of visibility via the enlisted characterization techniques: scanning electron microscopy (SEM), transmission electron microscopy (TEM) and atom probe tomography (APT).

3.2 Results and Discussion

3.2.1 Transmission Electron Microscopy

TEM has shown previously to be a useful technique for the evaluation of inclusions within single crystals.[90,93] Here, in bright field TEM (BF-TEM), high-aspect ratio nanorods with a width of ~100 nm can be visualized [Fig 3.1]. Gold nanoparticles can also be seen as dark circles in BF-TEM are also viewed in this image. These Au-NP appear to have diameters of ~10 nm. In a zoomed out image [Fig 3.1b], evidence suggests that's the Au-NP group near ends and edges of the nanorods, although this is not certain without tomography.

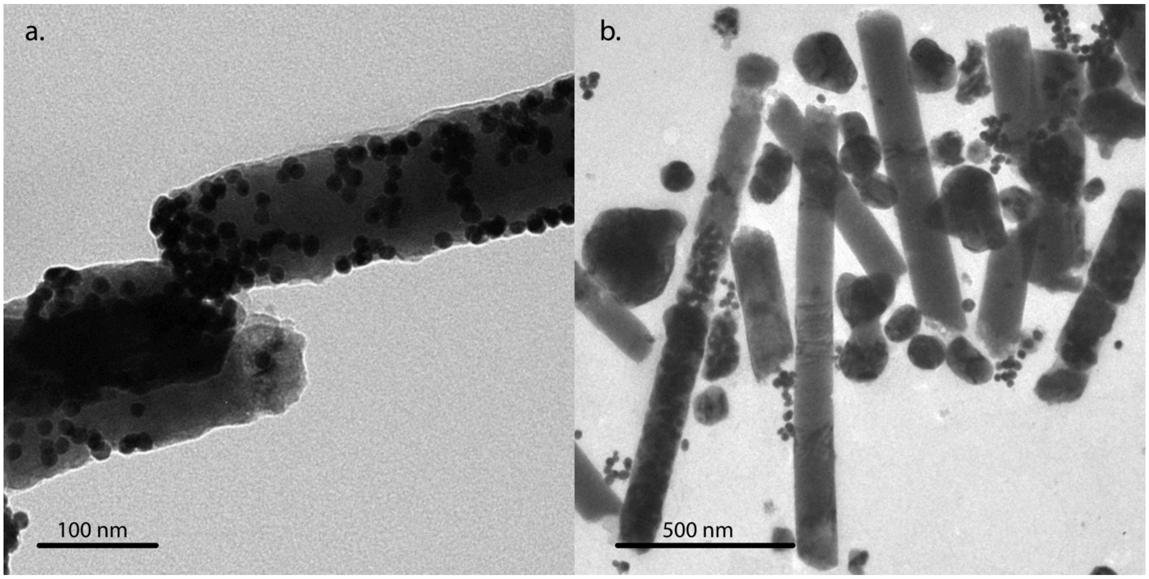

Figure 3.1| Bright Field TEM of Cu-NR; a| and b| show the composite construction of the Cu-NR with dark Au-NP embedded within the single crystal [Complements of Emily Asenath-Smith].

From a crystallography standpoint, it is of interest to understand the crystallographic direction at which growth in nano-confinement occurs. A few things complicate the determination of axis growth direction. Firstly, gold and Cu_2O have very similar lattice constants (4.1 and 4.3 Å, respectively). Secondly, without imaging directly down the axis of the nanorod, it is difficult to create certainty in terms of directionality via selected area diffraction (SAED). Perhaps focused-ion beam (FIB) sample preparation could be useful to create TEM samples oriented in this fashion. Further efforts are needed to systematically determine the long axis's crystallographic direction either via continued SAED of orthogonal diffraction across multiple tilt angles or on-axis sample preparation.

3.2.2 APT of Cu_2O Octahedron and Cuprite standards

Two independent cuprite samples were considered as standards for atom probe tomography purposes. First, we will consider a geological cuprite sample from the Wheal Phoenix locality (Cornwall, England, U.K.). Secondly, we characterized octahedral, single crystals of cuprous oxide (Cu-oct) that crystallize on the surface of the filter during Cu_2O-NR synthesis. These crystals grow to the size of roughly ~2 μm [Fig 3.2a], and in the absence of neither compartmentalization nor confinement exhibit 8 faceted sides edges. These crystal formation have been extensively studied via SEM and X-ray diffraction, previously.[97] These cuprite octahedrons (Cu-oct) samples were directly manipulated with a micromanupulator and welded directly atop APT micro-array posts [Fig 3.2b]. These were further sharpened into appropriately sized APT sample tips.

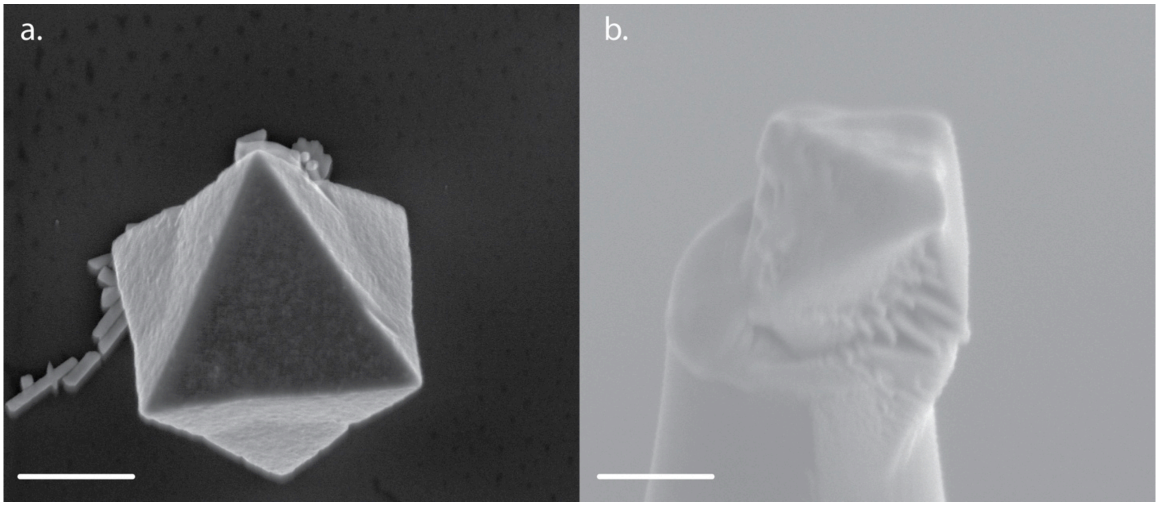

Figure 3.2| (both scale bars are 1 μm); a| Cu_2O octahedron; b| Cu_2O octahedron mounted on top of a Si-post

We begin by considering the spectra for these reference materials. Analyzing Fig 3.3 allows for recognitions of few differences and mysteries. The singularly charged Cu peak is the largest in both spectra, and to be expected, as Cu_2O is stoichiometrically 66.6at%

copper. APT of oxides yields a number of molecular fragments. In both spectra, we see CuO^{z+}, Cu_2O^+ and CuO_2^+ (where z can be 1 or 2). The spectrum of geological cuprite also displays a small peak at 44 Da, which is most likely CO_2^+ and is also identified in the Cu-oct spectrum. However, unlike the Cu-oct spectrum, which has a peak for CO^{2+} (14 Da), the geological cuprite does not display this peak, drawing into question the identity of the peak at 44 Da. The Cu-oct also shows a few additional C, N or Cl based peaks that are not seen in the geological cuprite. This suggests that the C, N and Cl are remnants from the solution processing of the Cu_2O, coming from citrate and other counter ions in solution. Of interest, at the same APT run-time parameters, we see a few distinct Cu-molecular fragments exclusively in the Cu-oct spectrum: CuO^{3+}, CuO_3^+. Further, a few mystery features exist in the spectra. At 60 and 61 Da, two sharp peaks are visible in the Cu-oct spectrum. Further, a hump centered on 79 Da is unidentified. This could be due to dissociation during flight, but its identity remains ambiguous.

3.2.3 Atom Probe Sample Preparation of Cu_2O Nanorods

The sub-field focused on the use of atom probe tomography of nanostructures has a number of tactics for sample preparation. These range from conventional to unconventional and include: FIB-liftout of sandwiched nanomaterials, deposition onto microarray APT sample arrays,[98] direct growth,[99] manipulator lift-out, etc. Due to the size, and solution processing of the Cu-NR two techniques were specifically explored. Firstly, manipulation with nanomanipulators was attempted to pick-up nanorods and atom probe them directly from the probe. Secondly, direct deposition onto pre-fabricated atom probe arrays and encapsulation in metal was employed.

Welding nanorods directly onto a tungsten probe has a few advantages. Most notably, the ability to select optimal samples and orient the nanorod with respect to the probe. This increases your useful field of view over the region of interest. However, the difficulty in FIB welding a nanorod directly onto a tungsten tip was quickly observed. These nanorods damage extremely readily due to ion beam exposure, requiring limited ion exposure or sub-optimal imaging settings. Perhaps the biggest difficulty is the inability to place the rod directly collinear with the axis of the tungsten probe. This creates an atom probe sample with a deflection in geometry. The inability to create complete collinearity [Fig 3.4a] means that when the sample is placed in a high electric field in the APT, stresses on the construct will maximize at the weld and cause fracture. It is nearly impossible to

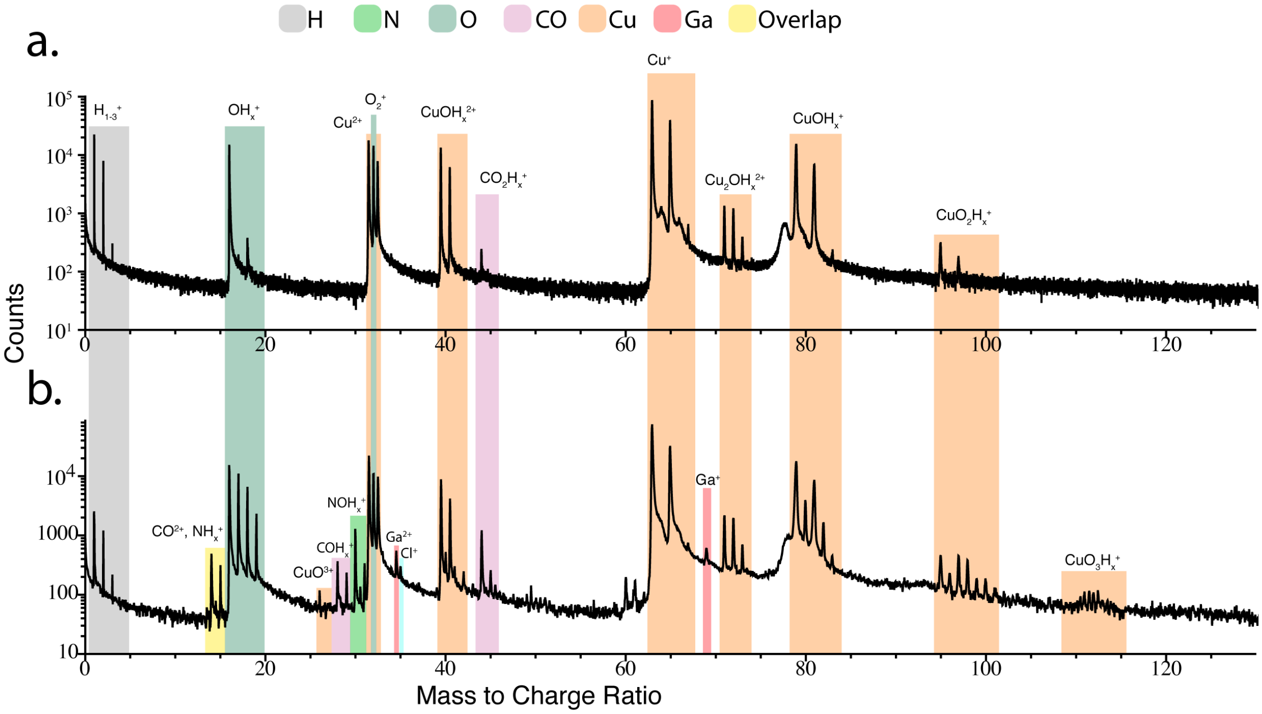

Figure 3.3| Spectra of Cu_2O standards at 10 pJ laser power for a| geological Cuprite at b| Cu-oct synthesized as a byproduct of nanorod fabrication.

produce high throughput in this fashion. Samples also commonly facture at the interface between the weld and the rod [Fig 3.4b] during pickup. All samples created in this way fractured, or yielded nonsensical atom probe data.

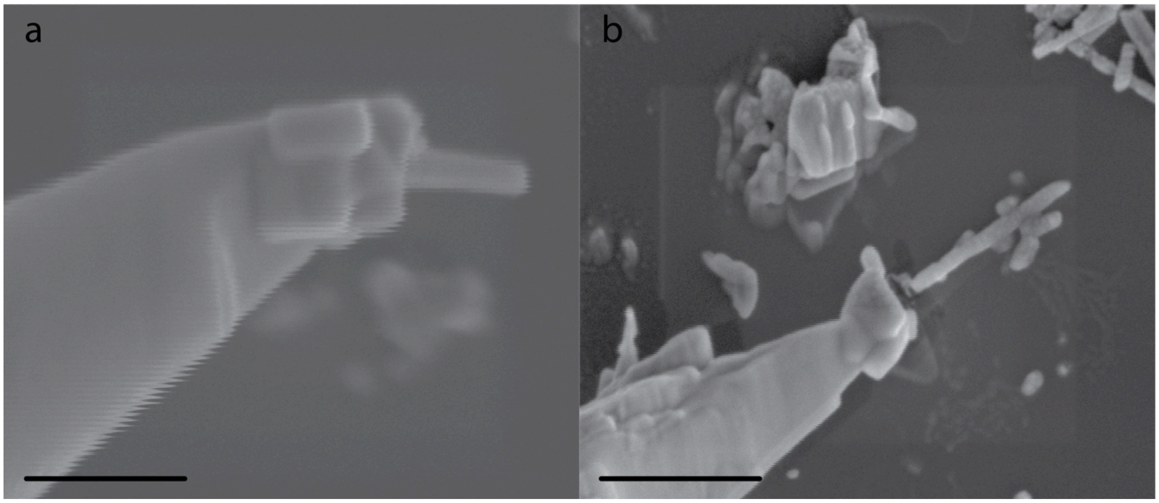

Figure 3.4| Attempts to micromanipulate Cu-NR with a tungsten tip (scale bars are 1 μm); a| Shows a successful pickup, but displays the lack of ability to create collinearity between the Cu-NR and the W-tip; b| Shows a common failure between the Cu-NR and the W-tip during pickup.

Direct deposition of nanorods directly onto APT arrays excels in a few places where direct pickup fails. By directly depositing nanorods onto Si posts, high throughput can be accomplished, creating ~18 tips per attempt. Unlike direct pickup, this technique has no selectivity for clean NR, or the ability to align the rod with respect to the atom probe sample axis. This technique is outlined pictorially in [Fig 3.5]. Briefly, (a) posts are coated (ion sputter) with ~100 nm of Pt and subsequently (b) ~15 nm of Pd. Palladium was used as a cover layer as it was found to adhere well to Cu-NR. Nanorods (c) are then deposited atop the posts and the entire coupon is baked in air to remove fragments from the track-etched membrane. Sample is then capped with ~150 nm of Pd (d) to encapsulate the NR. This was enough to protect and fill in the NR, but as it's a conformal coating, it was still possible to identify positions of NR. At this step, a protective cap of e-beam decomposed Pt (~1 μm) was used to protect the region of interest, and (e) conventional annular milling techniques were used to create a sharp (radius of ~ 100 nm) APT sample with a Pt cap.

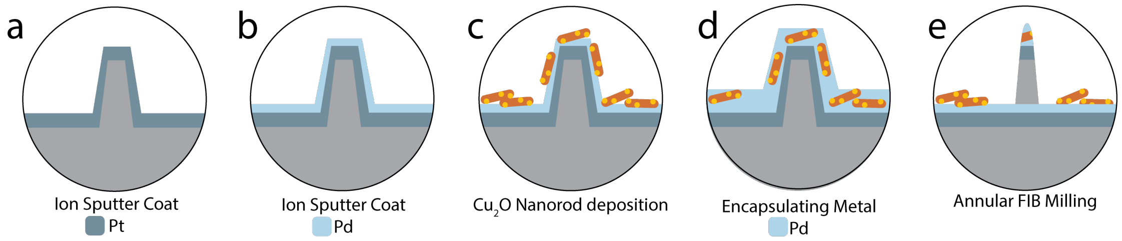

Figure 3.5| Sample preparation for direct deposition where a| Si-post APT array is coated with ~150 nm of ion sputter Pt, and subsequently b| coated with ~15 nm of Pd. This array is than coated in c| Cu-NR solution and heated in vacuum to 15˚C to remove excess organic. These Cu-NR are d| covered in a protective layer of Pd and e| milled into a APT tip.

3.2.4 Atom Probe Tomography of Cu$_2$O Nanorods

Preliminary results with the direct deposition method are reported. Due to the multiple layers and large carbon content located on the sides of the tips following deposition, a higher laser power (75 pJ) was found to yield the most ions during an APT run. This minimizes the applied voltage on the tip and the inherent stresses. As we will discuss, however, this does not yield ideal stoichiometry.

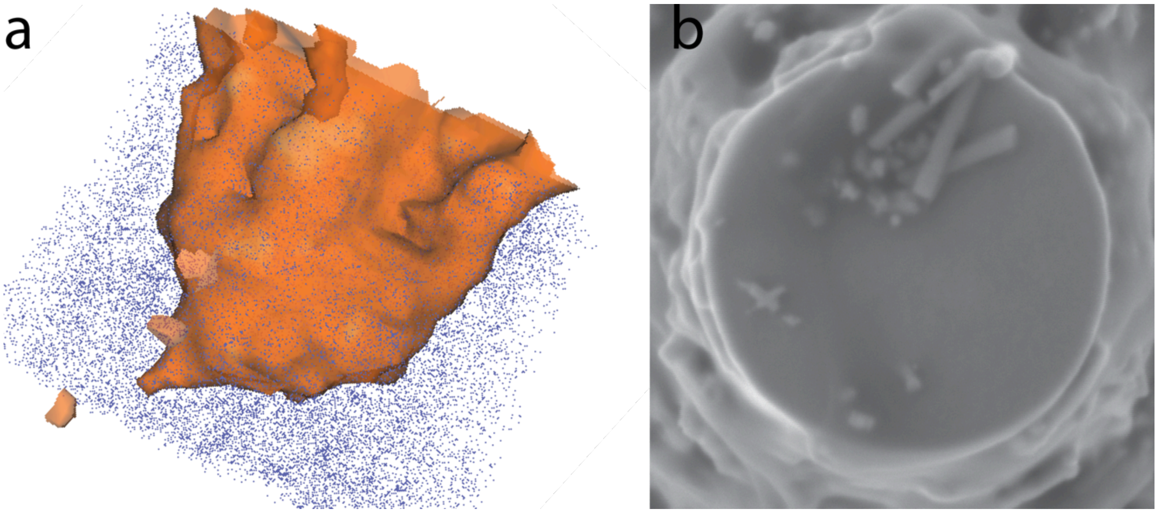

Figure 3.6| a| Preliminary APT results showing a Cu-NR clearly projecting into the Pd (blue circles), Isosurface is 63at% Cu (orange), no scale bar is drawn as reconstruction parameters are not well defined; b| SEM image of the sample prior to Pd coating.

Using an isoconcentration surface of 63 at% Cu, we can immediately recognize the Cu-NR shape perturbing into the field-of-view [Fig 3.6a]. If we compare this to the SEM image of the post taken prior to Pd coating [Fig 3.6b] we can begin to hypothesize which Cu-NR end that is probed by APT. Reconstruction values are unknown and complex for this system, so it is difficult to estimate the dimensions of the tip of the Cu-NR.

By analyzing the spectra for this sample [Fig 3.7a] we see the strong Cu^+ peaks as well as the recognizable Pd^+ and PdO^+ from the ion sputtered coating. Immediately these spectrum look distinct in comparison to Fig 3.5. This is due to the high laser power (75 pJ) used to analyze these samples. In the geological cuprite, large plateaus are seen through the high 20's and 40's Da, as well as surrounding the Cu^+ peak. At this high laser power, the bulk cuprite is likely unable to dissipate the power, leading to overheating and increased kinetic energy. Higher-powered laser pulses excite the sample tip with more energy, thus increasing the kinetic energy of the atoms at the tip. This higher energetic level reduces the necessary electric field required for field evaporation. This reduction in field reduces the nonspecific field evaporation, or background.

Further, at these high laser powers, as found in the magnetite samples explored in Chapter 1, we see a reduction in detected oxygen. Considering stoichiometric measurements against applied laser power [Fig 3.8], we see that in bulk, geological cuprite, at 75 pJ, we would observe 83.54 at% Cu and only 10.50 at% O. This poor compositional measurement is clearly due to the high laser power. At lower powers, below 50 pJ, we find that APT is capable of measuring accurate compositions. Future work should be conducted at lower laser powers (50 pJ) to ensure more accurate Cu-O measurements and decrease potential overheating of the sample tip.

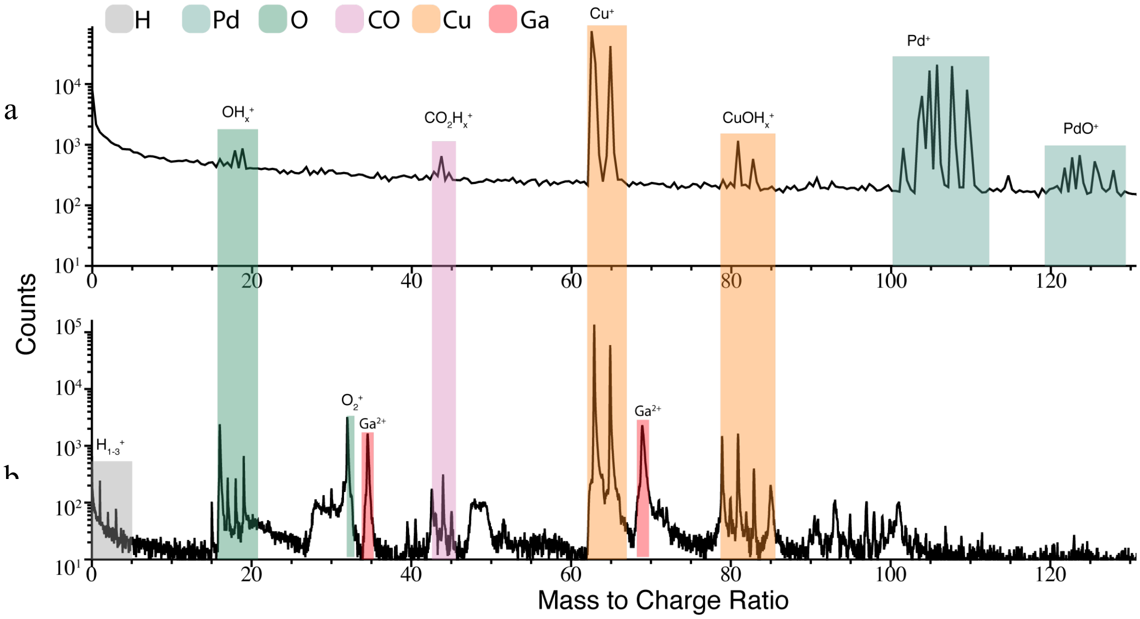

Figure 3.7| Spectrum for APT samples at 75 pJ for a| Cu-NR sample coated in Pd and b| geological Cuprite.

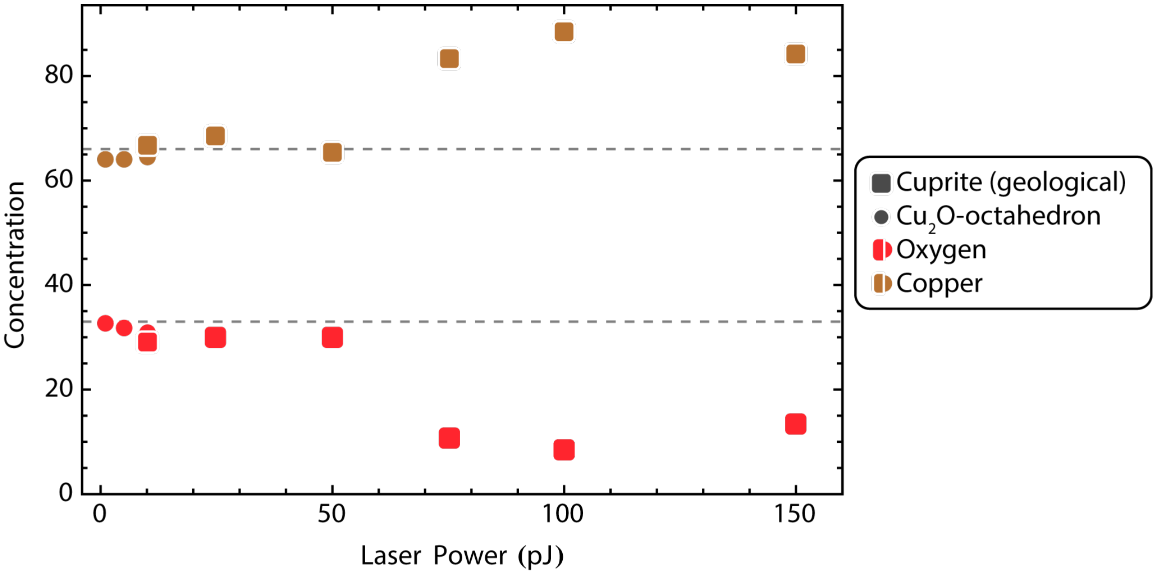

Figure 3.8| Shows APT measured composition for Cu and O (at%) in geological cuprite and Cu-oct. Horizontal dashed lines represent stoichiometrically expected at%.

3.3 Conclusion

This work shows the tremendous difficulty with analyzing nanomaterials with APT, especially when sample preparation of the original nanomaterial compounds the difficulty with additional foreign materials such as Cu-oct and carbon remnants from the track-etched membrane. Further, with preliminary data we show that the analysis of Cu_2O nanorods is plausible in APT, but to characterize the construct with a Au-NP, both entities must be included in the sample. TEM shows inhomogeneous distribution of Au-NP within the rod, which highlights this difficulty. In the geological magnetite samples analyzed, we see the ability in bulk to analyze buried interfaces of foreign/distinct material. However, if these are not distributed homogeneously, as in the case of Cu-NR, it becomes increasingly difficult to "get lucky" and uncover a nanoparticle. Additionally, we see the difficulty in analyzing nanorods which cannot be grown directly into a atom probe sample as done previously.[99] The fabrication of the Cu-NR as currently performed included a large fraction of Cu-oct and carbon-based remnants of the track-etched membrane. Additional steps should be taken to remove the octahedrons and the carbon membrane from the final sample preparation to ensure that potential APT sample tips are free from such unwanted intruders.

3.4 Materials and Methods

Note: portions regarding fabrication of Au-NP and Cu-NR used from work by Amanda Mae Uhl

3.4.1 Consumables

Gold (III) chloride trihydrate (99.99%, Aldrich); sodium citrate (Na_3Cit, Sigma-Aldrich); copper (II) sulfate pentahydrate (98%, Sigma-Aldrich); sodium hydroxide pellets (99.2%, Fisher); dichloromethane (DCM, 99.8%, Sigma-Aldrich); sodium borohydride (NaBH4, Sigma); cysteamine hydrochloride (98%, Sigma); polyvinylpyrrolidone (PVP, Sigma); ethanol (100%, Pharmco-Aaper); Epo-Tek 301 epoxy (Epoxy Tech-nology, Billerica, MA); CarbiMet II SiC grinding paper, Microcut SiC grinding paper, Metadi supreme polycrystalline aqueous diamond polishing suspension, Masterprep Alumina suspension, Trident polishing cloth, Chemomet polishing cloth (Buehler, Lake Bluff, IL); Conductive Liquid Silver Paint (Ted Pella, Redding, CA). Super Glue Cyanoacrylate Adhesive (3M, St. Paul, MN); Ultrapure Water (ρ=18.2 MΩ·cm) was prepared with a Barnstead Nanopure UF+UV ultrapure water purification system (Thermo-Fisher Scientific, Waltham, MA).

3.4.2 Citrate-Stabilized Gold nanoparticle Synthesis

Gold nanoparticles were synthesized using the Turkevich method, which produces citrate-stabilized gold nanoparticles.[100] Briefly, 50 mL of a 4.6 10^{-4} M $HAuCl_4$ solution was brought to a boil while stirring under reflux. Once boiling, 2.53 mL of 1% trisodium citrate (Na_3Cit) solution was added. The solution color progressed from yellow to ruby over the course of roughly five minutes. The solution was heated with continued stirring for 30 m. The solution was cooled for a 30 m and subsequently rinsed by dialysis into pH 10 (NaOH) deionized water with three exchanges over the course of 24 h.

3.4.3 Characterization of Au-NP

Hydrodynamic diameters of gold nanoparticles were characterized using dynamic light scattering (DLS) and surface charge using zeta-potential (Zetasizer Nano ZS, Malvern Instruments Ltd., Worcestershire, UK). The size of the Au-NP was targeted to be 20 nm. Crystallinity and size were further probed in bright field TEM (FEI Tecnai T12, FEI, Hillsboro, OR, USA). UV/Vis Spectroscopy (Spectramax Plus384 Absorbance Microplate Reader, Molecular Devices, LLC., Sunnyvale, CA, USA) was further used to determine peak absorbance of nanoparticles in solution.

3.4.4 Copper (I) Oxide Nanorod Synthesis

Cu_2O was synthesized using a method based on Benedict's test.[101] The basis of this reaction is the reduction of Cu^{2+} to Cu^{+} under basic conditions, where the role of citrate is to form a copper-citrate complex in order to prevent the precipitation of copper (II) hydrous phases when pH is increased. In our experiments, reduction was achieved by the vapor diffusion of hydrazine as a reducing agent. Track-etched membranes were impregnated with the Au-NP solution from *section 3.4.2*. These (particle-laden) track-etched membranes were placed into the basic, copper-citrate solution containing 2 mL of 0.068 M $CuSO_4$, 2 mL of 0.074 M Na_3Cit, and 2 ml of 0.12 M NaOH and degassed under vacuum for 30 m. Subsequently, N_2H_4 was introduced via vapor phase at 60°C. The vapor diffusion of N_2H_4 into the copper solution facilitated the crystallization of Cu_2O in the pores of the membrane. The reaction ran for 13 h during which the solution beginning at a blue-green and the membrane at light purple both became red-orange.

3.4.5 Membrane Cleaning & Dissolution

Following the reaction, the membranes were removed from the reaction vessel and cooled for 30 m. The membranes were then rinsed with water (3x) and EtOH (3x). The surface of the membrane was then gently scraped with the edge of a piece of parchment paper to remove crystals that were not attached to the surface. The track-etched membranes were dissolved with DCM. The nanorods were isolated by centrifugation and rinsing (DCM (3x)) by centrifugation.

3.4.6 TEM Characterization of Cu2O nanorods with Au-NP

Bright field TEM was conducted on a FEI Tecnai T12 (FEI, Hillsboro, OR, USA) by Emily Asenath-Smith.

3.4.7 Embedding, Grinding and Polishing — Geological Cuprite

Faceted crystals of Cuprite locality (Cornwall, England, UK) were embedded in Epo-Tek 301 epoxy and polymerized overnight at 25°C. Embedded samples were ground using progressively finer grits of Buehler SiC grinding paper (400, 600, 800 & 1200 grit). Ground samples were polished using 3 µm and 1.0 µm polycrystalline aqueous diamond polishing suspensions on a Buehler Trident polishing cloth. Finally, samples were rinsed with water and dried under flowing argon gas.

3.4.8 Mounting and Coating — Geological Cuprite

For SEM imaging, mounted samples were secured to an aluminum stub with cyanoacrylate adhesive, coated with ~5 nm of Pt with an Ion Beam Sputter Deposition and Etching System (IBS/e, South Bay Technologies, San Clemente, CA) operating at a base pressure of < 10^{-4} Pa and working pressure of 10^{-2} Pa Ar, with two ion guns operating at 9 kV and 3 mA per gun. The coating was grounded to the stub with conductive liquid silver paint.

3.4.9 Atom Probe Tomography Sample Preparation – Geological Cuprite

Samples for APT were prepared using the dual-beam SEM/FIB instrument (Helios Nanolab, FEI, Hillsboro, Oregon) using established protocols.[66] A rectangular strap of platinum (FIB-Pt) was deposited over a region of interest on the polished cross-section using the ion beam (30kV, 93pA) to locally decompose an organometallic precursor gas, (trimethyl)methylcyclopentadienyl-platinum $(CH_3)_3Pt(CpCH3)$, over a region of interest (2 x 25 μm) on a polished cross-section. A wedge of material below the Pt strap was cut out on three sides. The wedge was attached to an in-situ nano-manipulator (Omniprobe, Dallas, TX) using FIB-Pt before cutting the final edge free. 1-2μm wide segments were cut from the wedge and sequentially affixed to the tops of Si posts in an array (Cameca Scientific Instruments, Madison, WI) with FIB-Pt. Each tip was shaped and sharpened using annular milling patterns of increasingly smaller inner and outer diameters. The majority of the amorphized surface region and implanted gallium in the tip surface was removed by milling at 2 kV, 0.4 nA.

3.4.10 Atom Probe Tomography Sample Preparation – Octahedrons

Solutions of Cu-NR were deposited directly onto Si substrates (native oxide) and baked in a low vacuum at 150˚C for 24-36 h. Samples for APT were prepared using similar methods as section 3.4.9. Octahedrons, made as a byproduct of the Cu_2O nanorod fabrication, assumed to have crystallized without Au-NP and on the surface of the track-etch filter, were manipulated using an in situ nano-manipulator (Omniprobe, Dallas, TX) using electron beam Pt (e-Pt) deposition. As section 3.4.9, the electron beam (5 kV, 1.4 nA) was used to locally decompose an organometallic precursor gas, (trimethyl)methylcyclopentadienyl-platinum $(CH_3)_3Pt(CpCH3)$ to weld Cu_2O octahedrons to the nano-manipulator. Electron beam was used as FIB was found to damage these faceted micro-crystals. These octahedrons were placed directly on Si-posts in the micro-tip array (Cameca, Madison, WI, USA) [Fig 3.2b]. Using FIB-Pt, the octahedrons were mounted on one side to the posts, and the probe was cut free using the FIB (16 kV, 0.24 nA). The sample was welded equally on the other side and sharpening was conducted in a similar fashion as described in section 3.4.9.

3.4.11 Atom Probe Tomography Sample Preparation – Nanorods pickup

Samples from section *3.4.10* were also used to attempt to manipulate individual nanorods. These were mounted onto an *in situ* nano-manipulator (MM3A-EM micromanipulator, Kleindiek Nanotechnik GmbH, Reutlingen, Germany). Using a T-4-10 tungsten tip (GGB Industries, Naples, FL), Cu_2O NR with “mushroom caps” were identified, aligned (via stage rotation) and welded directly onto the very tip of the tungsten tip using e-Pt (5 kV, 1.4 nA). Minimal imaging with the FIB (15 kV, 45 pA) was performed to limit damage, but deemed necessary due to the 52° side angle view it offered. Tungsten tips, with nanorods, were removed from the nano-manipulator and crimped into Cu tubes. Tubes placed vertically in the stage of the FEI Dual-Beam to conduct post-processing to ensure proper welding on both sides of the tip with e-Pt and final cleaning.

3.4.12 Atom Probe Tomography Sample Preparation – Nanorods deposition

Atom probe arrays (Cameca, Madison, WI) were coated with ~150 nm of Pt and subsequently 15 nm of Pd with an Ion Beam Sputter Deposition and Etching System (IBS/e, South Bay Technologies, San Clemente, CA) operating at a base pressure of $< 10^{-4}$ Pa and working pressure of 10^{-2} Pa Ar, with two ion guns operating at 8 kV and 3 mA per gun. These samples were deposited with 1-2 uL of Cu-NR containing solution and the solvent was evaporated in air. The samples were then baked out in a low vacuum at 150˚C for 24-36 h. Samples were then imaged in the SEM (FEI, dual-beam Helios) at 5 kV and 1.4 mA to ensure that deposition of rods had occurred. In order to encapsulate and protect the rods, another ~100 nm of Pd was deposited in the IBS/e to encapsulate the rods on the tips. A 1 µm circular cap of platinum (e-Pt) was deposited over a region of each using the electron beam (5 kV, 1.4 nA) to locally decompose an organometallic precursor gas, (trimethyl)methylcyclopentadienyl-platinum $(CH_3)_3Pt(CpCH3)$. Each tip was shaped and sharpened using annular milling patterns of increasingly smaller inner and outer diameters, centered on the region of interest. The majority of the amorphized surface region and implanted gallium in the tip surface was removed by milling at 2 kV, 0.4 nA.

3.4.13 Atom Probe Tomography

Atom probe tomographic analyses were conducted in a Cameca local-electrode atom-probe tomograph (LEAP 4000XSi, Cameca, Madison, WI) using a pulsed laser ($\lambda = 355$ nm, 250 kHz, 1-150 pJ per pulse). The DC potential on a microtip during APT was controlled to maintain an evaporation rate 0.0025 ions per laser pulse. The base temperature of the microtip was maintained at 35 K and the ambient vacuum pressure was below 10^{-8} Pa.

3.4.14 Spectral Analysis

For visualization and analysis, peak integration intervals were defined manually for all elements and molecular fragments. These definitions are used to create the 3D reconstruction in Cameca's integrated visualization and analysis software (IVAS).

Compositional analysis was carried out using decomposition of peaks functionality in IVAS. Briefly, this software matches isotope ratios to the list of potentially input elements and molecular fragments, which the user provides.

3.4.15 Reconstruction Analysis

Three-dimensional reconstruction of APT data was performed using the Cameca integrated visualization and analysis software (IVAS) based on published algorithms, assuming a hemispherical tip shape.[102,103] Standard reconstruction parameters were used with an electric field-dependent tip radius (*r*).

4 CHARACTERIZATION OF DNA-WRAPPED CNTS USING ATOM PROBE TOMOGRAPHY

This section discusses initial attempts to characterize single-walled carbon nanotubes (SWCNTs) hybridized with single stranded DNA (ssDNA) using a laser pulsed atom probe. The bulk of this work has been conducted with assistance from the staff at the Center for Nanoscale Materials. Specifically Anirudha Sumant, as well as Lilliana Stan and Daniel Rosenmann, who were extremely important in attempts to grow SWCNTs specifically for this process. Karen DeRocher assisted through much of the process, and her efforts are credited as well. Parts of this work may be published in future publications or conference proceedings.

4.1 Introduction

Single-walled carbon nanotubes (SWCNTs) are widely acclaimed for their potential impact in technological fields due to impressive electrical,[104] mechanical,[105] optical,[106] and thermal[107] properties. Many of these impressive and unique emergent properties are created by SWCNT's nanoscale dimensionality and quasi-one-dimensional (1-D) structure.[108] These materials have found potential applications throughout a number of fields and applications, including as carbon nanotube field effect transistors (CNTFETs),[109] tissue engineering,[110] composites, sensors, energy storage,[111] bioelectronics, and biological material delivery.[112] The use of SWCNT in devices is highly attractive, particularly for flexible electronics.[113] As a community, we are limited in our ability to assemble SWCNTs into engineered devices, limiting the realization of the materials inherent potential.

Control of both assembly and carbon nanotube chirality/size is needed to create uniform, highly efficacious devices. Device performance could be dramatically improved by a) use of highly uniform SWNT and b) by controlled assembly of small numbers of SWNT into parallel arrays. Hybridization of SWCNTs with single stranded DNA oligonucleotides (ssDNA) creates an opportunity to solve this bifurcated problem concurrently.[114] Helical wrapping of single-stranded DNA (ssDNA) around SWCNTs is mediated via π-π stacking between bases and the nanotube.[114] This construct (CNT@DNA) displays a negative charge due to the phosphate groups of the wrapping DNA background, which facilitates dispersion in aqueous media. Molecular dynamic modeling of this process proposes a helical wrapping.[115] From the physics of this interaction, it logically follows that the nature of the wrapping is inherently sequence dependent, but also a function of the SWCNT's roll up vector (*n,m*), diameter, electronic properties and chirality.[116] The interactions create numerous possibilities including sorting by ion exchange, chromatography,[114] the incorporation of payloads such as cisplatin,[117] quantum dots,[118] and gene delivery.[119] At a slightly longer length-scale, the ability to create assembled three-dimensional constructs via DNA origami could great highly engineered CNTFET devises via ssDNA selection of SWCNTs.[120,121] Additionally, hybridization of SWCNTs with ssDNA allows for separation of similar CNTs by ion exchange chromatography.[114] The combination of remarkably improved CNT selection and assembly, suggests the possibility to assemble viable CNTFET devices via ssDNA control.[120]

Single-stranded DNA also opens a library of potential for modulating expressed chemistries on the CNT-based construct. Wrapping with DNA enables a number of possibilities such as non-covalent decoration with nanomaterials,[117] and deliver genetic materials.[122]

However, the wrapping of DNA around carbon nanotubes spatially and chemically poorly understood. With a number of variables: diameter, chirality, DNA sequence, and nanotube functionality, the affect of each on DNA wrapping remains poorly understood.[115] This lack of knowledge remains a considerable obstacle to logical design of CNT@DNA devices. The inability to image the physical wrapping of ssDNA around CNTs leaves the community dependent on computer simulation[123] to gauge the interaction of the aforementioned variables. There exists a significant need in the community for a single technique capable of accurately imaging the spatial, physicochemical wrapping of ssDNA around SWCNTs.

The gold standard in understanding the morphology of this construct is atomic force microscopy. However this technique is limited in spatial resolution by the sharpness of the cantilever tip,[124] and does not allow for chemical or 3D tomographical wrapping information. TEM has also been used in this regard but suffers from beam damage and other affects.[125] While simulations have greatly increased the fields understanding of the physical wrapping process,[123] further attempts to characterize and correlate with these findings is needed.

To characterize this hybrid material and the hetero-interface that dictates form, we propose to use Atom Probe Tomography (APT) to characterize the interface and nanostructure of these hybrid materials. Our group has shown atom probe tomography to be extremely valuable in characterizing organic-inorganic interfaces.[126]

4.2 Results and Discussion

4.2.1 AFM pickup of CNTs

The first concept explored for fabricating APT samples out of CNTs was to directly pick up SWCNTs onto an AFM tip [Fig 4.1]. This has been done previously with chemical vapour deposition (CVD) growth CNTs on a Si substrate.[127] This was attempted with numerous combinations of CNTs and DNA@CNTs dispersed onto Si substrates with no success. Using various dilutions of dichloromethane, acetone, ethanol and methanol, we attempted to use contact mode AFM to "pick-up" CNTs on to Si AFM tips. A myriad of problems including clumping, meniscus formation, and adhesion to the underlying substrate made this an incredibly frustrating technique. It is theorized that with CVD grown CNTs, the CNTs lie atop each other and interact less strongly with the Si substrate then in the case of deposited CNTs.

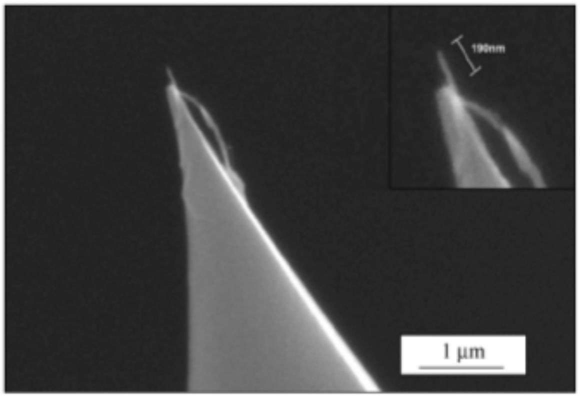

Figure 4.1 MWCNT picked up directly onto a Si AFM tip [Gibson, 2007]

4.2.2 CVD Growth of Vertically Aligned CNTs

Vertically aligned CNT (VACNT) forests have been grown previously with and without plasma to create well-aligned, long carpets or forests of CNTs.[128] We aimed to create VACNT atop Si-post APT arrays. Briefly, this multi-stage process begins with atomic layer deposition (ALD) of alumina [Al_2O_3], followed by e-beam evaporation deposition of a thin 2 Å Fe layer. These samples are then annealed *in situ* in a CVD, which is additionally capable of controlling the flow of ethylene [C_2H_4] at elevated temperature to feed the growth of VACNTs. In theory, these samples would be hybridized (or not) with ssDNA and encapsulated (potentially) in a protective metal through electroplating. These would be FIB milled into appropriate APT samples and characterized.

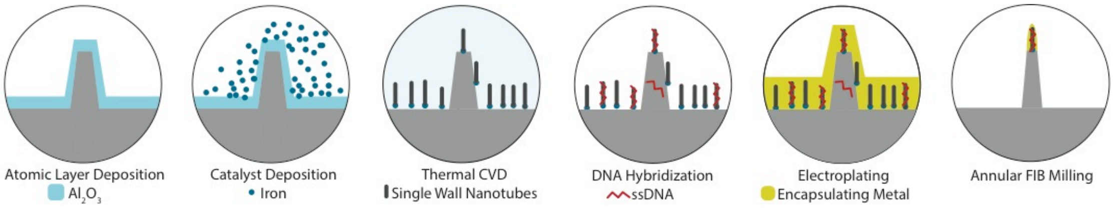
Atomic Layer Deposition
Al2O3
Catalyst Deposition
• Iron
Thermal CVD
Single Wall Nanotubes
DNA Hybridization
ssDNA
Electroplating
Encapsulating Metal
Annular FIB Milling

Figure 4.2 Schematic depiction of the CVD process for the fabrication of VACNTs. First, samples are coated with 14 nm of Al_2O_3, which is subsequently e-beam evaporator coated with a thin Fe layer. This substrate is annealed in the CVD chamber and a carbon-source gas is flowed through the chamber. These would be subsequently post-processed with ssDNA and a encapsulating metal to create a APT sample with the CNT aligned along the sample axis.

Unfortunately, at the facility that we used to grow these VACNTs, the recipes are not well defined as the facility generally grows graphene. So far, we have conducted multiple trials varying the annealing time, temperature, and growth time. The most promising result [Fig 4.3], shows low-density distribution of curled, MWCNT-looking objects. This result has not been reproduced and does not exhibit the expected dense CNT forest seen by others.[128] Further efforts must be taken to truly determine if the APT sample fabrication outlined here [Fig 4.2] would succeed. We have not conducted FTIR or other characterization techniques to describe this sample. Currently, we are attempting CVD growth with substrates with thicker (3 Å Fe layers) to increase the catalysis of CNTs.

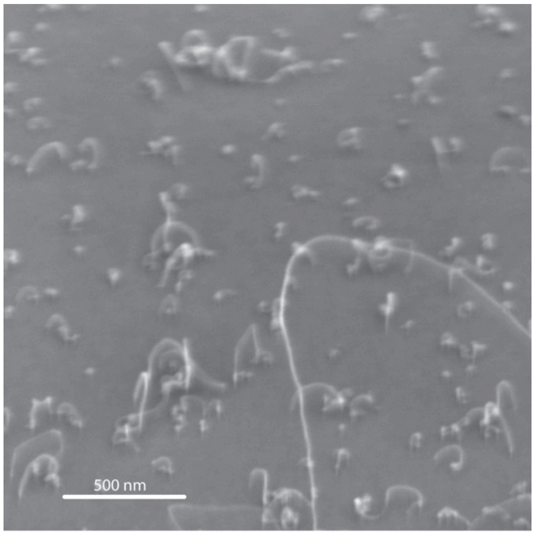

Figure 4.3| SEM of potential CNTs, annealed at 750˚C and grown for 10 min.

4.3 Conclusion

Preliminary work concerning the analysis of CNTs with APT is considered. Initial attempts to pick-up CNTs found to be quite discouraging. While pickup allows for characterization of the sample prior to sample fabrication, it suffers from low throughput and additional complications (as in Chapter 3). Additional work is needed to refine the recipes to grow VACNTs directly onto the APT arrays for APT analysis. It is theorized that the current Fe-catalysis layer is too thin, and we are currently manufacturing new samples with a thicker (3 Å) layer of Fe. Additionally, we are instigating a collaboration with Malte Bartenwerfer, Volkmar Eichhorn at Sergej Fatikow at the University of Oldenburg. Their work focuses on the nanorobotic assembly of AFM probes outfitted with MWCNTs. Discouraged by the low throughput and effort associated with the creation of AFM-CNT tips, they created an *in situ* manipulator for MWCNTs [Fig 4.4].[1] We are currently in initial stages of creating APT Si-post arrays with MWCNTs FIB-Pt welded on top of the plateau.

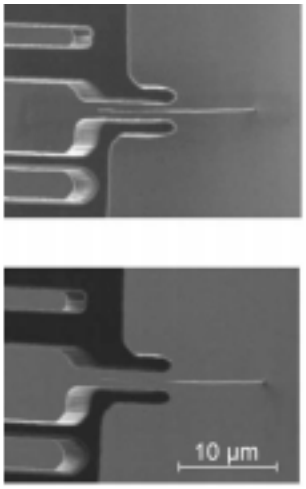

Figure 4.4| SEM image of the CNT gripper jaws.[1]

4.4 Materials and Methods

4.4.1 Deposition of Alumina

Silicon Wafers (Ted Pella), and atom probe arrays (Cameca, Madison, WI) were loaded into a Bench-Top Atomic Layer Deposition System (Gemstar-8, Arradiance Inc, Sudbury, MA). 100 cycles of a precursor gas [tri-methyl aluminium, $Al_2(CH_3)_6$] and water vapor at 100˚C resulted in a 14 nm film (unverified).

4.4.2 E-beam evaporation of Fe catalyst

ALD Si substrates were loaded into a Kurt Lester System Sputter and E-Beam Evaporator and 2 Å of Fe was deposited onto the surface. This work was conducted by Daniel Rosenmann, and is not further discussed here.

4.4.3 Chemical Vapor Deposition and Annealing

Si substrates were subsequently prepared for CVD by dicing with diamond blades into small squares (~1 cm^2). Diced pieces were placed onto quartz boats and placed inside of the quartz tube inside the PE-CVD (Atomate, Inc). Sample chamber was pumped down to 0.01 Torr. Samples were than annealed in an atmosphere of flowing Ar to a temperature of 750˚C for 10-15 min. The CVD process occurs by flowing a mixed atmosphere of ethylene, hydrogen and argon gas into the chamber at 750˚-800˚C for 20-40 min. During cooling and Ar gas is flowed over the samples.

4.4.4 Sample Imaging

Samples were imaged using the DualBeam scanning electron microscope (SEM) and focused ion beam (FIB) instrument (Helios NanoLab, FEI). SEM Imaging was conducted (5 kV, 1.4 nA) at various angles to access growth results.

4.4.5 AFM Characterization

Samples were further characterized using an Icon$^{©}$ Atomic Force Microscope (Bruker Biosciences Corp., Billerica, MA) and tapping mode Si tips (Bruker Biosciences Corp., Billerica, MA). Using pressure-sensitive tape (3M, Minneapolis, MN), carbon nanostructures were removed to allow for imaging the height of the growth product relative to the Si wafer.

REFERENCES

1 Eichhorn V., B. M., Fatikow S. *IEEE Transactions on Automation Science and Engineering* **9** (2012).

2 S.D. Sitzman, J. F. B., J.W. Valley. *American Mineralogist* **85**, 8 (2000).

3 Gordon, L. M., Tran, L. & Joester, D. Atom Probe Tomography of Apatites and Bone-Type Mineralized Tissues. *ACS nano* **6**, 10667-10675 (2012).

4 Graham, J. W. V. a. C. M. Cryptic Grain-Scale Heterogeneity of Oxygen Isotope Ratios in Metamorphic Magnetite. *Science* **259**, 4 (1993).

5 Price, G. D. *Physics of Earth and Planetary Interiors* **23**, 11 (1980).

6 J.W. Valley, C. M. G. *Contributions to Mineralogy and Petrology* **109**, 15 (1991).

7 R. J. Harrison, R. E. D.-B., A. Putnis. *PNAS* **99**, 6 (2002).

8 K.R. Kuhlman, R. L. M., T.F. Kelly, N.D. Evans, M.K. Miller. Fabrication of specimens of metamorphic magnetite crystals for field ion microscopy and atom probe microanalysis. *Ultramicroscopy* **89**, 8 (2001).

9 J. M. Eiler, J. W. V., C. M. Graham, L.P. Baumgartner. *American Mineralogist* **80**, 8 (1995).

10 K. Mezger, B. A. v. d. P., E.J. Essene, A.N. Halliday. *The Journal of Geology* **100**, 111 (1992).

11 J.W. Valley, J. R. O. N. *Contributions to Mineralogy and Petrology* **85**, 16 (1984).

12 Putnis, R. J. H. a. A. The Magnetic Properties of Crystal Chemistry of Oxide Spinel Solid Solutions. *Surverys in Geophysics* **19**, 461 (1999).

13 M.E. Evans, D. K., W. Williams, M. Winklhofer. *Journal of Geophysical Research* **111**, 7 (2006).

14 Price, G. D. *Geology Magazin* **116**, 6 (1979).

15 Nickel, E. H. *The Canadian Mineralogist*, 9 (1958).

16 Mogensen, F. A Ferro-Ortho-titanate ore from Södra Ulvön. *Geolgiska Föreningen i Stockholm Föhandlingar* **68**, 578 (1946).

17 Price, G. D. *American Mineralogist* **66**, 8 (1981).

18 Seidman, D. N. *Annual Revies Materials Research* **37**, 34 (2007).

19 T.F. Kelly, D. J. L. Atoim Probe Tomography 2012. *Annual Revies Materials Research* **42**, 30 (2012).

20 B. Gault, M. P. M., F. de Geuser, G. Tsafnat, A.L. Fontaine, L.T. Stephenson, D. Haley, S.P. Ringer. Advances in calibration of atom probe tomographic reconstruction. *105* (2009).

21 J.W. Valley, A. J. C., T. Ushikubo, D.A. Reinhard, D.F. Lawrence, D.J. Larson, P.H. Clifton, T.F. Kelly, S.A. Wilde, D.E. Moser, M.J. Spicuzza. Hadean age for a post-magma-ocean ziron confirmed by atom-probe tomography. *Nature Geoscience* **7**, 4 (2014).

22 Joester, L. M. G. a. D. Nano-Scale Chemical Tomography of Buried Organic-Inorganic Interfaces in Chiton Tooth. *Nature* **469**, 3 (2011).

23 Sitzman, S. D. *Microstructural Controls on Oxygen Isotope Distribution, Rheology, and Magnetic Properties in Metamorphic Magnetite* Masters of Science thesis, University of Wisconsin, Madison, (1996).

24 M.F. Ashby, L. M. B. *Phil. Mag.* **8** (1963b).

25 C.L. Lawson, R. J. H. *Solving least squares problems*. Vol. 161 (Prentice-Hall, 1974).

26 Oberdorfer C., S. P., Reinke C., Schmitz G. *Microscopy and Microanalysis* **13**, 342-346 (2007).

27 Gordon L.M., T. L., Joester D. *ACS Nano* **6**, 10667-10675 (2012).

28 E.A. Marquis, N. A. Y., D.J. Larson, M.K. Miller, R.I. Todd. *Materials Today* **13**, 34-36 (2010).

29 Kuchibhatla S.V.N.T, S. V., Prosa T.J., Adusumili P., Arey B., Buxbaum A., Wang Y.C., Tessner T., Ulfig R., Wang C.M., Thevuthasan S. *Nanotechnology* **23**, 215704 (2012).

30 Valley J.W., C. A. J., Ushikubo T., Reinhard D.A., Lawrence D.F., Larson D.J., Clinton P.H., Kelly T.F., Wilde S.A., Moser D.E., Spicuzzo M.J. *Nature Geoscience* **7**, 219 (2014).

31 Y.M. Chen, T. O., M. Kodzuka, K. Morita, K. Hono. *Scripta Materilia* **61**, 693-696 (2009).

32 Gault B.P., M. M. P., Cairney J.M., Ringer S.P. *Atom Probe Tomograhy*. (Springer Science+Busines Media, LLC, 2012).

33 Saxey, D. W. *Ultramicroscopy* **111**, 473-479 (2011).

34 Bachhav M., D. R., Danoix F., Hannoyer B., Ogale S., Vurpillot F. *Ultramicroscopy* **111**, 584-588 (2011).

35 McMurray S.G., G. B. P., Diercks D. *Microscopy and Microanalysis* **17**, 758-759 (2011).

36 Larson D.J., A. R. L., Lawrence D.F., Prosa T.J., Ulfig R.M., Reinhard D.A., Clifton P.H., Gerstl S.S.A., Bunton J.H., Lenz D.R., Kelly T.F., Stiller K. *Microscopy and Microanalysis* **14**, 1254-1255 (2008).

37 Gault B.P., M. M., La Fontaine A., Moody M.P., Shariq A., Cerezo A., Ringer S.P. Smith G.D.W. *Journal Applied Physics* **108**, 044904 (2010).

38 A.J.W., M. *Phil. Mag.* **43**, 803-814 (1981).

39 John W. Anthony, R. A. B., Kenneth W. Bladh, and Monte C. Nichols,. (ed Mineralogical Society of America) (Chantilly, VA 20151-1110, USA).

40 Kimberly R. Kuhlman, P. G. C., Richard L. Martens, Thomas F. Kelly, Derren Dunn, Neal D. Evans, Michael K. Miller. Nanogeology of Metamorphic Magnetite using Three-Dimensional Atom Probe and Focused Ion Beam Secondary Ion Mass Spectroscopy. (Jet Propulsion Laboratory, 2001).

41 Kimberly Kuhlman, J. W. Method of sample preparation for atom probes and source of specimens. USA patent US20040056195 A1 (2004).

42 Blakemore, R. Magnetotactic Bacteria. *Science* **190**, 399-379 (1975).

43 Joseph L Kirschvink, J. L. G. Biogenic magnetite as a basis for magnetic field detection in animals. *Biosystems* **13**, 181-201 (1981).

44 P. Berteisen, W. G., M.B. Madsen, K.M. Kinch, S.F. Hviid, J.M. Knudsen, H.P. Gunniaugsson, J. Merrison, P. Nornberg, S.W. Squyres, J.F. Bell III, K.E. Herkenhoff, S. Gorevan, A.S. Yen, T. Myrick, G. Klingelöfer, R. Rieder, R. Gellert. Magnetic Properties Experiments on the Mars Exploration Rover Spirit at Gusev Crater. *Science* **305**, 827-829 (2004).

45 David J. Barger, E. R. D. S. Origin of supposedly biogenic magnetite in the Martian meteorite Allan Hills 84001. *Proceedings of the National Academy of Science* **99**, 6556-6561 (2002).

46 M.K. Miller, K. F. R., K. Thompson, R. Alvis, D.J. Larson. Review of Atom Probe FIB-Based Specimen Preparation Methods. *Microscopy and Microanalysis* **13**, 8 (2007).

47 Miller, M. K. Atom Probe Tomography. *Kluwer Academic* (2000).

48 P. Bas, A. B., B. Deconihout, D. Blavette. A general protocol for the reconstruction of 3D atom probe data. *Applied Surface Science* **87**, 6 (1995).

49 L.A. Giannuzzi, F. A. S. A review of fobused ion beam milling techniques for TEM specimen preparation. *Micron* **30**, 7 (1999).

50 Robinson, C. *et al.* The chemistry of enamel caries. *Critical Reviews in Oral Biology & Medicine* **11**, 481 (2000).

51 "Dental Spending Growth Resumes". (2012).

52 Gurenlian, J. R. *Journal of Dental Hygiene*, 4-11 (2007).

53 (ed Center for Disease Control) (cdc.gov).

54 H. Cohen, D. L. *Journal of Canadian Dental Association* **67**, 10 (2001).

55 Dental Enamel. (West Sussex, England, 1997).

56 Gerth, H. *Dental Materials* **23**, 1521 (2007).

57 H Toots, R. P. *Contributions to Geology* **18**, 1 (1979).

58 Silverstone, L., Saxton, C., Dogon, I. & Fejerskov, O. Variation in the pattern of acid etching of human dental enamel examined by scanning electron microscopy. *Caries research* **9**, 373-387 (1975).

59 Shulin, W. *Electron Microscopy Reviews* **2**, 1-16 (1989).

60 Featherstone, J. Remineralization, the natural caries repair process—the need for new approaches. *Advances in Dental Research* **21**, 4-7 (2009).

61 Terpstra, R. & Driessens, F. Magnesium in tooth enamel and synthetic apatites. *Calcified tissue international* **39**, 348-354 (1986).

62 Landi E., L. G., Proietti L., Tampieri A., Sandri M., Sprio S. *J Mat Sci: Mat in Med* **19**, 239-247 (2006).

63 Driessens, F. C. M. *Bulletin des Societes Chimiques Belges* **89**, 663-689 (2010).

64 Ankudinov, A., Ravel, B., Rehr, J., Conradson, S. *Physical Review B* **58**, 7565 (1998).

65 Dien, L., Mingsheng, P. & Murata, T. Coordination and local structure of magnesium in silicate minerals and glasses; Mg K-edge XANES study. *The Canadian Mineralogist* **37**, 199-206 (1999).

66 Miller, M. K., Russell, K. F. & Thompson, G. B. Strategies for fabricating atom probe specimens with a dual beam FIB. *Ultramicroscopy* **102**, 287-298 (2005).

67 Miller, M. K. *Atom Probe Tomography: Analysis at the Atomic Level.* (Plenum Pub Corp, 2000).

68 Bas, P., Bostel, A., Deconihout, B. & Blavette, D. A general protocol for the reconstruction of 3D atom probe data. *Applied Surface Science* **87**, 298-304 (1995).

69 Fadeev, I., Shvorneva, L., Barinov, S. & Orlovskii, V. Synthesis and structure of magnesium-substituted hydroxyapatite. *Inorganic materials* **39**, 947-950 (2003).

70 Ravel, B. & Newville, M. ATHENA, ARTEMIS, HEPHAESTUS: data analysis for X-ray absorption spectroscopy using IFEFFIT. *Journal of Synchrotron Radiation* **12**, 537-541 (2005).

71 Antao, S. M., Mulder, W. H., Hassan, I., Crichton, W. A. & Parise, J. B. Cation disorder in dolomite, CaMg (CO3) 2, and its influence on the aragonite+ magnesite↔ dolomite reaction boundary. *American Mineralogist* **89**, 1142-1147 (2004).

72 Doness, W. Crystal structure refinement of huntite, CaMgr (COr) 4, with X-ray powder data. *American Mineralogist* **71**, 163-166 (1986).

73 Calvo, C. & Gopal, R. The crystal structure of whitlockite from the Palermo Quarry. *Am. Mineral* **60**, 120-133 (1975).

74 Hughes, J. M., Cameron, M. & Crowley, K. D. Structural variations in natural F, OH, and Cl apatites. *American Mineralogist* **74**, 870-876 (1989).

75 Rehr, J. J. & Albers, R. Theoretical approaches to x-ray absorption fine structure. *Reviews of Modern Physics* **72**, 621 (2000).

76 Reeder, R. J., Lamble, G. M. & Northrup, P. A. XAFS study of the coordination and local relaxation around Co2+, Zn2+, Pb2+, and Ba2+, trace elements in calcite. *American Mineralogist* **84**, 1049-1060 (1999).

77 Harries, J., Hukins, D., Holt, C. & Hasnain, S. Conversion of amorphous calcium phosphate into hydroxyapatite investigated by EXAFS spectroscopy. *Journal of crystal growth* **84**, 563-570 (1987).

78 Holt, C. *et al.* Preparation of amorphous calcium-magnesium phosphates at pH 7 and characterization by X-ray absorption and fourier transform infrared spectroscopy. *Journal of crystal growth* **92**, 239-252 (1988).

79 A.O. Musa, T. A., M. Carter. *Journal of Solar Energy Materials Solid Cells* **51** (1998).

80 J Zhang, J. L., Q Peng, X Wang, Y Li. *Chemical Materials* **18** (2006).

81 S. Brittman, Y. Y., N.P. Dasgupta, S. Kim, P. Yang. *Nano Letters* (2014).

82 Yiwei Tan, X. X., Qing Peng, Heng Zhao, Taihong Wang, Yadong Li. *Nano Letters* **7** (2007).

83 Agekyan, V. T. *Physical Status Solidi Annuls* **43** (1977).

84 Agekyan, V. T. *Physica Status Solidi* **43**, 11-42 (1977).

85 T Minami, Y. N., T. Miyata. *Apply Physics Express* **6**, 044101 (2013).

86 Y.S. Lee, J. H., M.T. Winkler, S.C. Siah, S.B. Kim, R.G. Gordon, T. Buonassisi. *Journal of Materials Chemistry A* **1**, 15416 (2013).

87 A. Paracchino, J. C. B., J.E. Moser, E. Thimsen, M. Graetzel. *Journal Physical Chemistry* **116**, 7341-7350 (2012).

88 Y. Sui, W. F., H. Yang, Y. Zeng, Y. Zhang, Q. Zhao, Y. Li, X. Zhou, Y. Leng, M. Li, G. Zou. *Crystal Growth and Design* **10**, 99-108 (2010).

89 C.L Kuo, R. C. W., J.L Hang, C.P. Liu, C.K. Wang, S.P. Chang, W.H. Chu, C.H. Wang, C.H. Tu. *Nanotechnology* **20**, 365603 (2009).

90 LM Gordon, D. J. *Nature* **469** (2011).

91 C.-H. Wu, R. K., C. Tester, W. Gu, D. Jang, J. Greer, B. Lai, S. Chen, C. Sun. M. Balasubramanian, D. Joester. *Microscopy and Microanalysis* **19**, 1632-1633 (2013).

92 Hanying Li, H. L. X., David A Muller, Lara A Estroff. *Science* **326** (2009).

93 HY Li, H. X., ME Kunitake, EC Keen, DA Muller, LA Estroff. *Advanced Functional Materials* **21**, 2018 (2011).

94 H Zhou, S. W. *ACS Nano* **2** (2008).

95 C Lu, L. Q., H Cong, X Wange, J Yang, D Zhang, J Ma, W Cao. *Chemistry of Materials* **17**, 5218 (2005).

96 R. Munoz-Espi, A. C., G Wegner. *Crystal Growth and Design* **7**, 1584 (2007).

97 Siegfried M.J., C. K.-S. *Advanced Materials* **16**, 1743-1746 (2004).

98 L.M. Gordon, M. J. C., D. Joester. *Microscopy and Microanalysis* **19**, 952-953 (2013).

99 J.R. Riley, R. A. B., Q. Li, H.D. Espinosa, G.T. Wang, L.J. Lauhon. *ACS Nano* **6**, 3898-3906 (2012).

100 J. Kimling, M. M., B. Okenve, V. Kotaidis, H. Ballot, A. Plech. *Journal of Physical Chemistry B* **110**, 15700 (2006).

101 Benedict, S. R. *Journal of Beiological Chemistry* **5**, 485 (1909).

102 Miller, M. K. *Kluwer Academic* (2000).

103 P. Bas, B. D., D. Blabette. *Applied Surface Science* **87** (1995).

104 Q. Cau, J. A. R. *Advanced Materials* **21**, 29-53 (2009).

105 A.B. Dalton, S. C., E. Munoz, J.M. Razal, V.H. Ebron, J.P. Ferraris, J.N. Coleman, B.G. Kim, R.H. Baughman. *Nature* **423**, 703 (2003).

106 S.M. Bachilo, M. S. S., C. Kittrell, R.H. Hauge, R.E. Smalley, R.B. Weisman. *Science* **298** (2002).

107 J. Hone, M. W., C. Piskoti, A. Zettl. *Physical Review B* **59**, R2514-R2516.

108 Jariwala D., S. V. K., Lauhon L.J., Marks T.J., Hersam M.C. *Chem Soc Rev* **42**, 2824-2860 (2013).

109 Javey A., G. J., Wang Q., Lundstrom M., Dai H. *Nature* **424**, 654-657 (2003).

110 B. S. Harrison, A. A. *Biomaterials*, 344-353 (2007).

111 R.H. Baughman, A. A. Z., W.A. de Heer. *Science* **297**, 787-792 (2002).

112 W. Yang, P. T., J.J. Gooding, S.P. Ringer, F. Braet. *Nanotechnology* **18** (2007).

113 Meitl M.A., Z. Y., Gaur A., Jeon S., Usrey M.L., Strano M.S., Rodgers J.A. *NanoLetters* **4**, 1643-1647 (2004).

114 M. Zheng, A. J., E.D. Semke, B.A. Diner, R.S. McILean, S.R. Lustig, R.E. Richardson, N.G. Tassi. *Nature Materials* **2**, 338-342 (2003).

115 X. Tu, M. Z. *Nano Research*, 185-194 (2008).

116 X. Tu, S. M., A. Jagota, M. Zheng. *Nature* **460**, 250-253 (2009).

117 G.N. Ostojic, J. R. I., M.C. Hersam. *Langmuir* **24**, 9784-9789 (2008).

118 J.F. Campbell, I. T., H.H. Thorp, D.A. Erie. *JACS* **130**, 10648-10655 (2008).

119 D. Cai, C. A. D., T.B. Potochky, F.J. Dufort, Z. Huang, D. Blair, K. Kempa, Z.F. Ren, T.C. Chilies. *Nanotechnology* **18** (2007).

120 A.P. Eskelinen, A. K., T.K. Kaltiaisenaho, M.Y. Timmermans, A.G. Nasibulin, E.I. Kauppinen, P.Torma. *Small*, 746-750 (2011).

121 Z. Zhao, Y. L., H. Yan. *Organic and Biomolecular Chemistry* (2013).

122 Sing R. Pantarotto D., M. D., Chaloin O., Hoebeke J., Partidos C.d., Briand J.-P., Prato M., Bianco A., Kostarelos K. *JACS* **127**, 4388-4396 (2005).

123 A.N. Enyashin, S. G., G. Seifert. *Nanotechnology* **18**, 245702 (2007).

124 Zhong W., O. G., Tomanek D. *Europhysical Letters* **15**, 49-54 (1991).

125 Wang J., L. G., Jan M.R. *JACS Communication* **126**, 3010-3011 (2003).

126 L.M. Gordon, D. J. *Nature* **469**, 194 (2011).

127 Gibson C.T., C. S., Roberts C.J. *Ultramicroscopy* **107**, 118-1122 (2007).

128 Bell M.S., T. K. B. K., Lacerda R.G., Milne W.I., Hash D.B., Meyyappan M. *Pure Applied Chemistry* **78**, 1117-1125 (2006).